Article

Stabilizer-free bismuth nanoparticles for selective polyol electrooxidation

Weiran Zheng,
Yong Li, Chui-
Shan Tsang, Pui-
Kin So, Lawrence
Yoon Suk Lee

lawrence.ys.lee@polyu.edu.hk

Highlights

Stabilizer-free bismuth nanoparticles (Bi NPs) are synthesized by laser ablation

Bi NPs show activity toward polyol electrooxidation, breaking C-C bond

The *in situ* generated Bi(V) is essential for the electrocatalytic oxidation

Unlike Bi polycrystal, surface oxide layers do not inhibit the activity of Bi NPs

Article

Stabilizer-free bismuth nanoparticles for selective polyol electrooxidation

Weiran Zheng,[1] Yong Li,[1] Chui-Shan Tsang,[2] Pui-Kin So,[2] and Lawrence Yoon Suk Lee[1,3,4,*]

SUMMARY

Bismuth is the least toxic element among heavy metals, an outstanding advantage for environmental and health considerations. Yet, utilizing bismuth as anodic electrocatalyst is hindered by the formation of a spreading $Bi(OH)_3$ inhibitor layer during the anodic process. Herein, we report that bismuth nanoparticles, produced using laser ablation, can avoid such drawbacks. The production of Bi(V) species assists polyol electrooxidation. For glucose, instead of the commonly reported gluconic acid as the product, the Bi(V) species enables highly selective oxidation and C–C bond cleavage to produce arabinonic acid, erythronic acid, and eventually glyceric acid. We not only generate high-valent Bi(V) species for catalytic applications, especially for bioelectrocatalysis where the less toxic bismuth is highly appreciated, but also present Bi nanoparticle as a highly selective electrocatalyst that can break C–C bond. We believe that Bi electrocatalyst can find broader applications in electrochemical biomass conversion and electrosynthesis.

INTRODUCTION

Bismuth, a post-transition metal element in group 15 of the periodic table, has been recently praised as "the magic element" after being overlooked for decades (Kanatzidis et al., 2020). Such a shift in research interest is mainly due to the miscellaneous coordination and bonding types enabled by the stereochemically active $6s^2$ lone-pair electrons of the bismuth atom and its broad valence states from reduced −3 to oxidized +5 assisted by the three p-orbital electrons. Such flexible nature of bismuth has made bismuth-based materials promising for electrocatalysis.

However, compared with the well-studied transition metal-based materials, the electrochemical applications of bismuth are rarely reported. After the pioneering studies of its fundamental electrochemistry reported in the 1970s and the 1980s (Williams and Wright, 1976, 1977; Wrona and Galus, 1980), it is only recently that bismuth-based materials (metal and oxides) have started to regain researchers' attention due to their unexpected high catalytic activity in the electrochemical reduction of carbon dioxide (Deng et al., 2019; Gong et al., 2019; Li et al., 2020; Medina-Ramos et al., 2017; Zhang et al., 2019) and nitrogen (Li et al., 2019; Wang et al., 2019; Yao et al., 2020), both of which involve the cathodic properties of bismuth atoms at low-valent states. Nevertheless, the utilization of its high-valent states under anodic conditions, such as Bi(III) and Bi(V), for the electrocatalytic oxidation process has not been demonstrated yet.

The enabling of bismuth-based materials for electrooxidation catalysis is especially critical for many bioelectrochemical applications because bismuth and its compounds generally show much lower toxicity than other transition metal-based ones (Nordberg; et al., 2015). Glucose electrooxidation, for example, is one of the most extensively studied bioelectrochemical reactions due to its importance in biosensing and energy conversion (Brouzgou and Tsiakaras, 2015; Heller and Feldman, 2008). The oxidation of glycerol also poses a great interest in the community of biomass conversion. Recent results demonstrated that both activity and selectivity of glycerol electrooxidation on conventional noble metal electrocatalysts, such as Pd and Pt, can be significantly improved by the Bi adatoms on their surface (de Souza et al., 2019, 2020; Garcia et al., 2017). Yet, the electrocatalysts based on earth-abundant elements, such as Cu (Zheng et al., 2019a), Co (Madhura et al., 2020), and Ni (Chen et al., 2016), are preferred due to their low cost. In these systems, an M^x/M^{x+1} ($x = 2$ for Cu and Ni; $x = 3$ for Co) redox cycle (Zheng et al., 2019b) is often proposed as the mechanism. Yet, their high toxicity toward cells and proteins cannot be ignored. On the other hand, bismuth shares a similar redox cycle of Bi(III)/Bi(V), which has been put into application in recent homogeneous catalysis (Planas et al., 2020). Such information leads us to wonder whether Bi alone can act as the electrocatalyst for polyol electrooxidation.

[1]Department of Applied Biology and Chemical Technology and the State Key Laboratory of Chemical Biology and Drug Discovery, The Hong Kong Polytechnic University, Hung Hom, Kowloon, Hong Kong SAR, China

[2]University Research Facility in Life Science, The Hong Kong Polytechnic University, Hung Hom, Kowloon, Hong Kong SAR, China

[3]Research Institute for Smart Energy, The Hong Kong Polytechnic University, Hung Hom, Kowloon, Hong Kong SAR, China

[4]Lead contact

*Correspondence: lawrence.ys.lee@polyu.edu.hk

https://doi.org/10.1016/j.isci.2021.102342
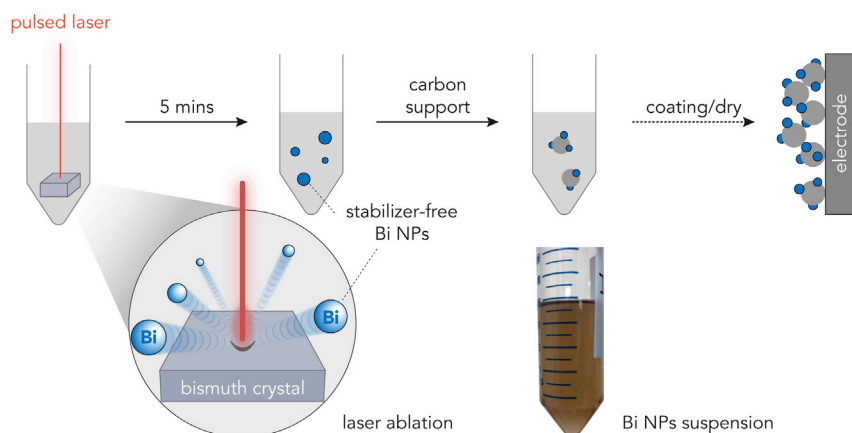
Scheme 1. Illustration of the laser ablation for Bi NPs production and the Bi NPs/AC-coated electrode preparation

The key to enabling the electrocatalytic oxidation ability of bismuth-based materials is to generate Bi(V) species. The desired Bi(0)-Bi(III)-Bi(V) pathway, however, has not been found among the previous anodic studies on bulk bismuth (Wrona and Galus, 1980). Instead of continuous oxidation to its high-valent states, a higher potential led to the production of a spreading and thickening $Bi(OH)_3$ layer from the surface to the inner lattice, which also acted as an inhibitor and hindered both electron transport and mass diffusion (Vivier et al., 2001; Williams and Wright, 1976, 1977).

Decreasing the size of the bismuth structure to nanometers seems to be a reasonable tactic to avoid the drawbacks caused by the micrometer levels of bismuth hydroxide formation. However, bismuth metal nanoparticles (NPs) are highly susceptible to oxidation upon exposure to air due to their vulnerable p-orbital electrons, making the preparation of sub-10-nm bismuth NPs very challenging. Currently, their synthesis relies heavily on hydrothermal methods, which involve stabilizers/capping agents on the particle's surface to lower the surface energy (Xia et al., 2014; Yarema et al., 2010). The existence of such agents, however, is known to block specific active sites, obstruct reactant(s) adsorption, change the reaction path, and alter the electronic properties of surface atoms dramatically (Heuer-Jungemann et al., 2019; Phan and Nguyen, 2017). Therefore, the obtaining of stabilizer-free bismuth NPs is essential to understanding its intrinsic electrocatalytic properties without interferences from other aspects.

Here, we present the preparation of stabilizer-free sub-10 nm Bi NPs using laser ablation. The differences between the electrochemical behaviors of Bi NPs and polycrystals (PCs), which lie in the ability of further oxidation to generate Bi(V) species on the NPs' surface, are discussed comprehensively. The Bi(III)-Bi(V) redox cycle enables glucose electrocatalytic oxidation on Bi NPs and C–C cleavage to produce C5, C4, and C3 hydrocarbon compounds. These results mark one of the first examples of using Bi NPs as catalysts for electrocatalytic oxidation.

RESULTS AND DISCUSSION

Preparation and characterization of Bi PCs and NPs

We employed two forms of elemental Bi for electrochemical studies: PCs and NPs. The Bi PCs-coated electrode was fabricated following a previously reported electrodeposition method by cathodically treating a glassy carbon electrode (GCE) in Bi^{3+}-containing acidic electrolyte (see transparent methods and Figure S1 for related data) (Sandnes et al., 2007).

The stabilizer-free Bi NPs were prepared via pulsed laser ablation in the liquid phase (PLAL), which had been demonstrated to be effective for other colloidal NP preparations (Amendola and Meneghetti, 2009; Zheng et al., 2020). As illustrated in Scheme 1 (for experimental setup, see Figure S2), a bulk Bi crystal was irradiated in deoxygenated isopropyl alcohol by a pulsed laser (Nd:YAG Q-switched, λ = 1,064 nm, 650 mJ, frequency = 10 Hz). Once the laser impacted the surface, a few ultrafine particles were emitted from the irradiated spot, causing the colorless solution to change to light gray within 5 min, indicating the formation

of a particle suspension (see Video S1). The well-established PLAL mechanism can be described as a combination of plasma generation and quenching. As the laser interacts with the Bi surface, a localized high-temperature plasma consisting of atoms and NPs is generated. After leaving the irradiation zone, such plasma is subsequently quenched by the surrounding liquid environment to form NPs (Zeng et al., 2012). Compared with conventional hydrothermal methods (Heuer-Jungemann et al., 2019), no stabilizer (or capping agent) is required in the PLAL process, ensuring a clean NP surface.

On the other hand, the absence of any stabilizer on the surface means high surface energy of the generated NPs, which often results in aggregation and Ostwald ripening (Heuer-Jungemann et al., 2019). To minimize these undesirable phenomena, the NPs suspension was immediately mixed with activated carbon (AC) support (Scheme 1) to immobilize the Bi NPs.

Figure 1A shows the optical image of the as-prepared Bi PCs-coated GCE, featuring numerous crystals at the micrometer scale (mainly 7–20 μm) anchoring on the smooth glassy carbon surface. Atomic force microscopy (AFM) image (Figure 1B) reveals the typical step formation on the surface of the crystal, a characteristic trait of Bi as a hopper crystal: quicker edge growth than facial crystallization (Cereceda-Company and Costa-Kramer, 2018). Meanwhile, the AFM (Figure 1C) and transmission electron microscopy (TEM, Figure 1D) images of the laser-treated sample confirm the successful preparation of Bi NPs, where the aggregation of the high surface energy NPs is also evident. A high-resolution TEM image of a single NP is presented in Figure 1E alongside the atomic model (three-dimensional [3D] and projection) of a Bi NP (Crystallography Open Database [COD] ID: 7123351, space group: R-3m) (Wei et al., 2019). The hexagonal projection matches well with the elemental Bi model, and the real atomic arrangement agrees with the projected Bi atomic pattern (region highlighted by red dotted frame), validating the production of elemental Bi NPs by PLAL. The size distributions of Bi NPs (see Figure S3 for low-magnification TEM image) and PCs are shown in Figure 1F, with the mean diameters of 9.6 nm and 11.4 μm, respectively.

Further structural information can be provided by the X-ray diffraction (XRD) patterns of Bi PCs and NPs, as shown in Figure 1G. The standard (PDF#44-1246) and simulated XRD profiles of elemental Bi and its ambient oxide form (alpha-Bi_2O_3: PDF#41-1449) are also provided for comparison. Electrochemically deposited Bi PCs show peaks that match well with both standard and simulated patterns. The Bi NPs exhibit two additional peaks at 26.77° and 33.05° (marked with *) in addition to the peaks assigned to elemental Bi and the broad signal between 15° and 35° attributed to amorphous AC. These two signals can be attributed to the (111) and (121) peaks of alpha-Bi_2O_3, which are produced by the inevitable oxidation of high surface energy Bi NPs when exposed to ambient oxygen.

Electrochemistry of Bi PCs and NPs

Understanding the fundamental electrochemistry of Bi PCs and NPs is beneficial for further electrocatalysis discussions. As the following glucose electrooxidation is performed in an alkaline electrolyte (0.1 M KOH aqueous solution), the discussion here regarding the electrochemical behavior of both Bi samples is limited to the alkaline conditions.

We used mainly two methods, cyclic direct current voltammetry (DCV, or CV for short) and Fourier transformed large-amplitude alternating current voltammetry (FTACV), to study the electrochemical behaviors. Briefly, CV is a well-established method that shows current responses caused by potential sweep on the electrode (Figure 2A), whereas FTACV, a relatively new technology developed by Alan M. Bond and co-workers, highlights the fast surface electron transfer processes (Zhang et al., 2018). Unlike the linearly increased potential in CV, a sinusoidal wave is applied onto the potential ramp in FTACV (Figure 2B). After the Fourier transform, the current response can be resolved to multiple frequency domains. In general, the higher domains (third and higher) are only related to the fast electron transfer and catalytic steps, not the slow mass transfer involved steps. FTACV can provide critical insights into the electrochemical processes as it is free of any background current. The following parts of this article will mainly rely on CV and FTACV results to provide an overall image of the electrochemical behaviors of bismuth.

Figures 2C and 2D show the continuous CV plots of Bi PCs and NPs from 1 to 100 cycles at a scan rate of 10 mV s^{-1}. The Bi NPs show larger double layer capacitance than Bi PCs, mainly due to the additional AC as well as the smaller particle size.
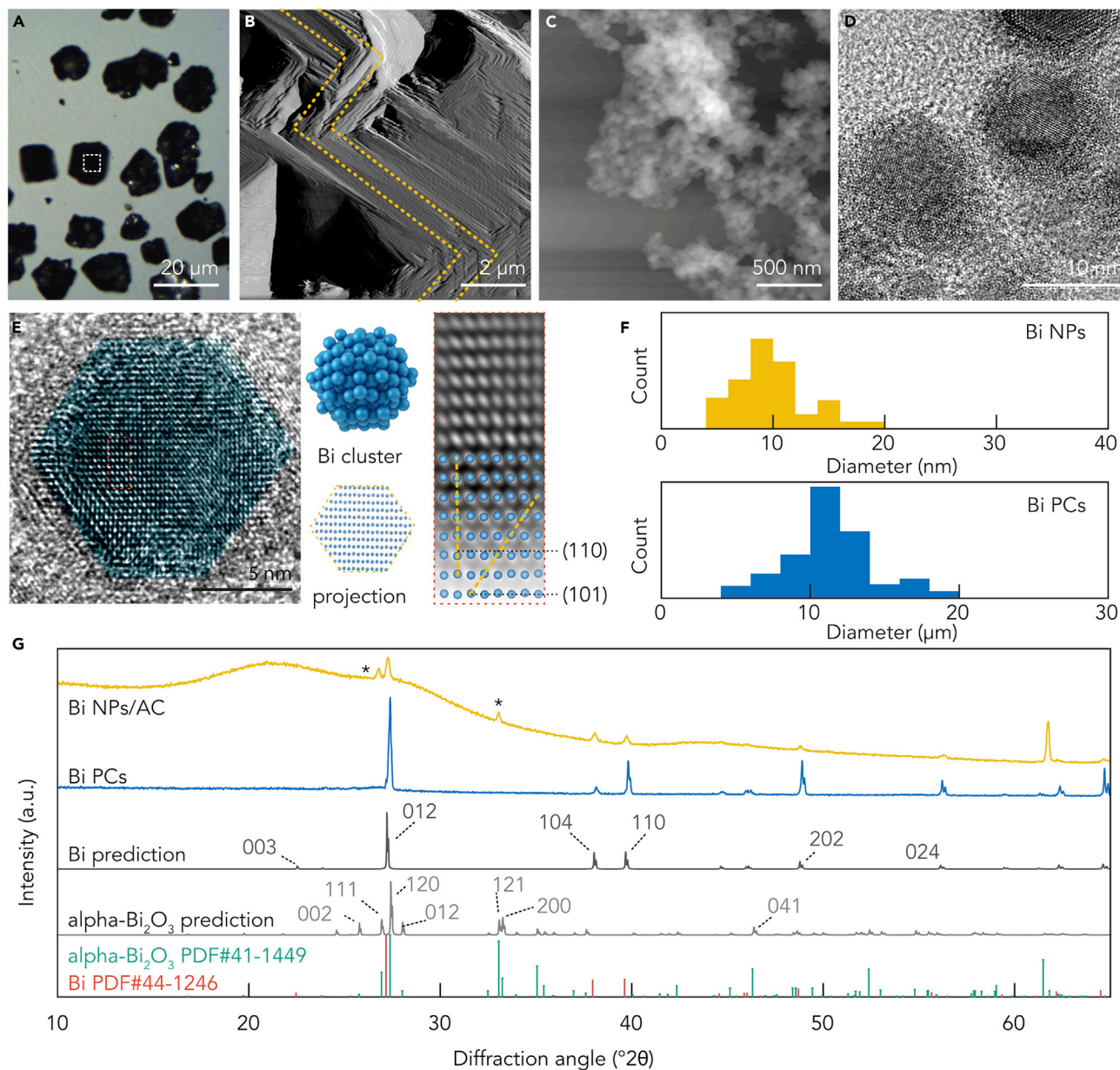
Figure 1. Morphologic and structural characterization of Bi PCs and NPs

(A) Optical image of cathodically deposited Bi PCs on GCE surface.

(B) AFM image of the selected Bi PC's surface (white box in A). The yellow dashed line outlines the crystalline surface boundary.

(C) AFM image of the aggregated spherical Bi NPs.

(D) TEM image of Bi NPs.

(E) High-resolution TEM image of a single Bi NP (highlighted in blue color). The atomic model and projection of a Bi NP is shown on the right, together with the real and matching simulated atomic arrangement.

(F) Size distribution of Bi NPs (from TEM images) and Bi PCs (from optical images).

(G) XRD patterns of Bi PCs and Bi NPs/AC samples. The predictions of Bi and alpha-Bi_2O_3 are generated using VESTA software with the structural models (for Bi, COD ID: 7123351; for alpha-Bi_2O_3, COD ID: 1526458). The standard patterns (Bi: PDF#44-1246; apha-Bi_2O_3: PDF#41-1449) are compared.

The anodic scan of the Bi PCs-coated electrode reveals a distinct oxidation peak A_1 centering at 0.42 V (versus RHE, the same below) and a broad peak A_2 from 0.51 to 0.65 V followed by an oxidation plateau. Vivier et al. (2000, 2001) described that all anodic signals within this potential range are related to the oxidation of Bi(0) species to Bi(III) species as follows:
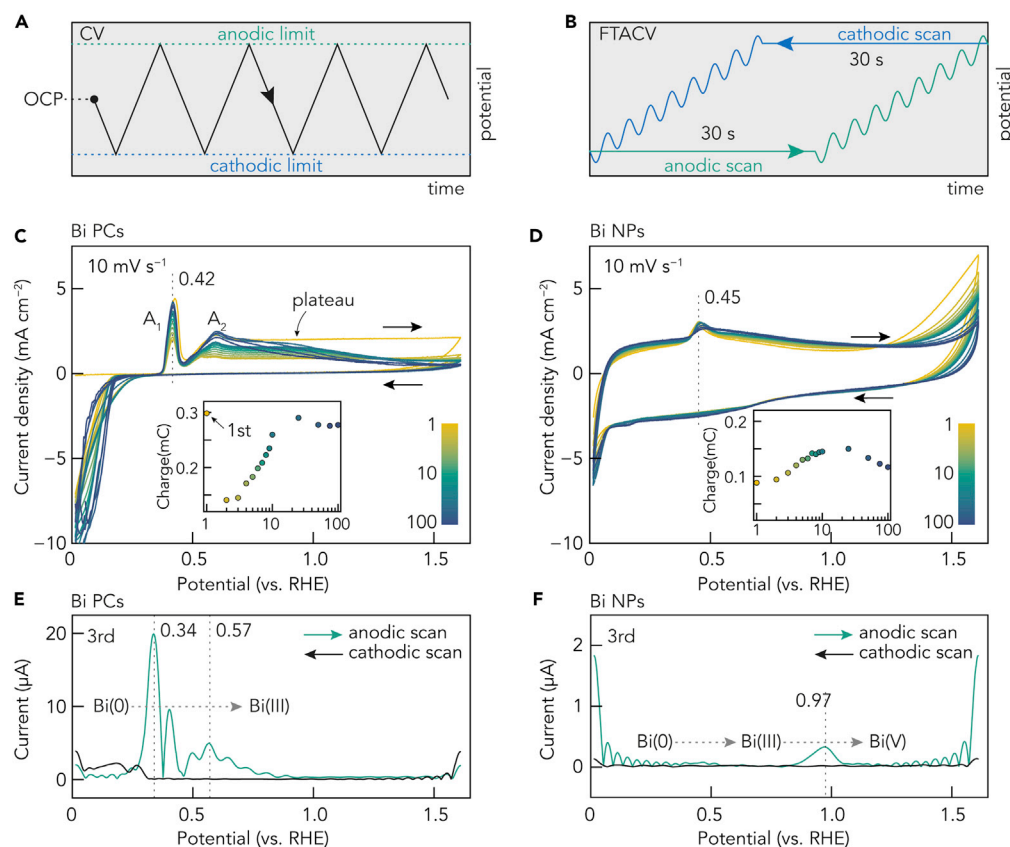
Figure 2. Electrochemistry of Bi PCs and NPs in 0.1 M KOH electrolyte
(A and B) Potential sequence used for (A) CV and (B) FTACV.
(C and D) Continuous CV plots (1, 2, …, 10, 25, 50, 75, 100) of (C) Bi PCs and (D) Bi NPs/AC. The scan rate is 10 mV s^{-1}. The insets show the correlation between the anodic peak (at *ca.* 0.4 V) charge and the cycle number.
(E and F) The third harmonic components of the FTACV plots of (E) Bi PCs and (F) Bi NPs/AC during the anodic and cathodic scans.

$$Bi^0 \rightarrow Bi^+ + e^- \tag{1}$$

$$3Bi^+ \rightarrow Bi^{3+} + 2Bi^0 \tag{2}$$

$$Bi^{3+} + 3OH^- \rightarrow Bi(OH)_3 \tag{3}$$

In other words, a fast electron transfer reaction (Reaction 1) is followed by two relatively slow chemical processes (Reactions 2 and 3). It should be noted that besides the electron transfer, such processes also involve a structural transition (structural models as shown in Figure S4) from metallic Bi(0) to Bi(OH)$_3$ (or BiOOH), and eventually to Bi$_2$O$_3$ at open circuit potential (OCP) (Vivier et al., 2001). Comparing the Raman spectra of the Bi-coated electrode before and after anodic treatment (see Figure S5) confirms the formation of alpha-Bi$_2$O$_3$, as indicated by the trait of O–Bi–O bands between 300–600 cm^{-1} (Betsch and White, 1978; Vila et al., 2012). Despite the fact that the reactions are the same, distinct peaks result from Bi atoms in different environments. The A$_1$ peak is associated with the oxidation of Bi(0) atoms at the BiPCs/electrolyte interface, whereas A$_2$ is related to the bulk Bi(0) atoms that are not directly exposed on the surface (Vivier et al., 2000). The observation that the total anodic charge of A$_2$ and the plateau is much larger than that of A$_1$ supports such an explanation because Bi PCs have more bulk atoms than the surface ones. As the surface/local OH$^-$ is consumed by A$_1$, the local pH decreases, and the oxidation potential of sublayer Bi shifts to a higher value (formation of A$_2$). The formation of the surface Bi(OH)$_3$ (and eventual Bi$_2$O$_3$) further hinders the diffusion of OH$^-$ from the bulk electrolyte into the Bi sites, causing the plateau. The cathodic scan shows the reduction current of Bi(III) to Bi(0) from 0.25 to 0 V.

The continuous CV study of Bi PCs shows an ever-changing profile from 1 to 100 cycles. The first cycle is of particular interest because it shows the highest oxidation signal of all three regions: A_1, A_2, and plateau. Such signals, however, decline significantly in the second cycle, whereas further cycling causes a gradual increment of all peaks. Following the previous explanation, these results indicate that the electron-accessible Bi atoms' population drops significantly after merely one CV cycle of the fresh Bi PCs and recovers slowly. The oxidation charge of the A1 peak (shown as the inset of Figure 2C) quantifies the surface Bi atoms where 10 cycles recover 85% of the initial. Nevertheless, Bi PCs are not electrochemically stable.

Figure 2D shows the continuous CV plots of the Bi NPs, revealing a different story. An oxidation peak at 0.45 V is evident, followed by a minor broad signal between *ca.* 0.5 and 0.8 V. Similar to the Bi PCs, the former peak can be assigned to the oxidation of surface Bi(0) and the following signal to bulk atoms. The much higher current density at 0.45 V is understandable because the NPs have a much higher surface-to-bulk atomic ratio than PCs. However, another oxidation signal appears from *ca.* 1.2 V, indicating further oxidation of Bi(III), most likely to the unstable Bi(V) species (Espinosa et al., 1991; Pourbaix, 1974), posing the most significant difference between the Bi NPs and PCs. As the cycle number increases, the oxidation charge of the surface Bi(0) increases gradually from 0.09 to 0.15 mC after 10 cycles. It stabilizes at 0.11 mC after 100 cycles, indicating the same trend of the surface atoms' population. Therefore, the Bi NPs are much more electrochemically stable than the PCs form.

The difference between NPs and PCs can be further revealed by the scan rate-dependent CVs (see Figure S6). At a low scan rate (5 mV s^{-1}) where diffusion factors are negligible, the separation between the anodic and cathodic peak potentials is *ca.* 0.28 V, showing a clear sign of irreversible behavior of Bi PCs, an observation that is also supported by the shifting peak potential of both anodic peaks with rising scan rates. Notably, the high scan rate (100 mV s^{-1}) produces an abnormally low current. This is most likely due to the accumulated inhibiting Bi_2O_3 layer created by the continuous cycles. The Bi NPs-coated electrode shows a similar anodic/cathodic peak separation (*ca.* 0.30 V). However, unlike PCs, the current grows with increasing scan rate, showing no inhibitor accumulation.

FTACV, as mentioned previously, can reveal the fast electron-transfer process of a coupled electrochemical reaction. Figure 2E presents the third harmonic components of both the anodic and cathodic scan of the Bi PCs-coated electrode. Two anodic peaks, which are centered at 0.34 and 0.57 V, are revealed, similar to its CV profile, whereas higher potential (>0.7 V) shows no signal. Thus, both anodic peaks are related to immediate electron transfer steps (Reaction 1), yet further oxidation (the plateau in Figure 2C) involves diffusion. Unlike the PCs, the FTACV results of the Bi NPs (Figure 2F) indicate a minor signal from 0.3 to 0.5 V and a distinct peak centering at 0.97 V. Despite the similar oxidation peaks suggested by the CV (0.42 V in Figure 2C and 0.45 V in Figure 2D), the oxidation of Bi(0) in the Bi NPs is most likely diffusion-controlled. Wrona and Galus (1980) suggested an alternative path different from V. Vivier's using a Bi Hg electrode:

$$Bi^0 + 2OH^- \rightarrow Bi(OH)_2^+ + 3e^- \tag{4}$$

As the nanoscale NPs are similar to Bi atoms dispersed in Hg, we believe that Reaction 4 is more suitable than Reaction 1 to describe electrooxidation of the Bi NPs. Meanwhile, the prominent peak at 0.97 V, which is not found in Figures 2E, is related to the Bi(III) to Bi(V) oxidation. During the cathodic scan of both samples, the current signals are significantly reduced, meaning that the electrochemical reduction follows different routes and is diffusion limiting, a topic that is beyond our focus here.

Glucose electrooxidation on Bi PCs and NPs

With the electrochemical behaviors of Bi PCs and NPs understood, the electrocatalytic activity of both materials toward glucose electrooxidation is studied, and the results are shown in Figure 3. With 2 mM glucose in the electrolyte, Bi PCs show no distinguishable oxidation signal from 0.7 to 1.6 V apart from slight intensity changes of Bi(0) species (inset of Figure 3A). The peak current of A_1 drops, and A_2 grows. As both peaks are attributed to the same reaction, these changes are likely to be caused by the coordination between glucose and surface Bi(0) atoms (Wenkin et al., 2002), resulting in more stable Bi(0) species with higher oxidation potential. Bi NPs, on the other hand, exhibit an oxidation signal at *ca.* 1.46 V after adding 2 mM glucose to the electrolyte (Figure 3B), which can be attributed to glucose electrooxidation on Bi. Apart from that, the differential anodic signal (subtracting the anodic scan by the glucose-free scan) indicates extra charge output in the Bi(0) oxidation region, presumably for glucose adsorption.
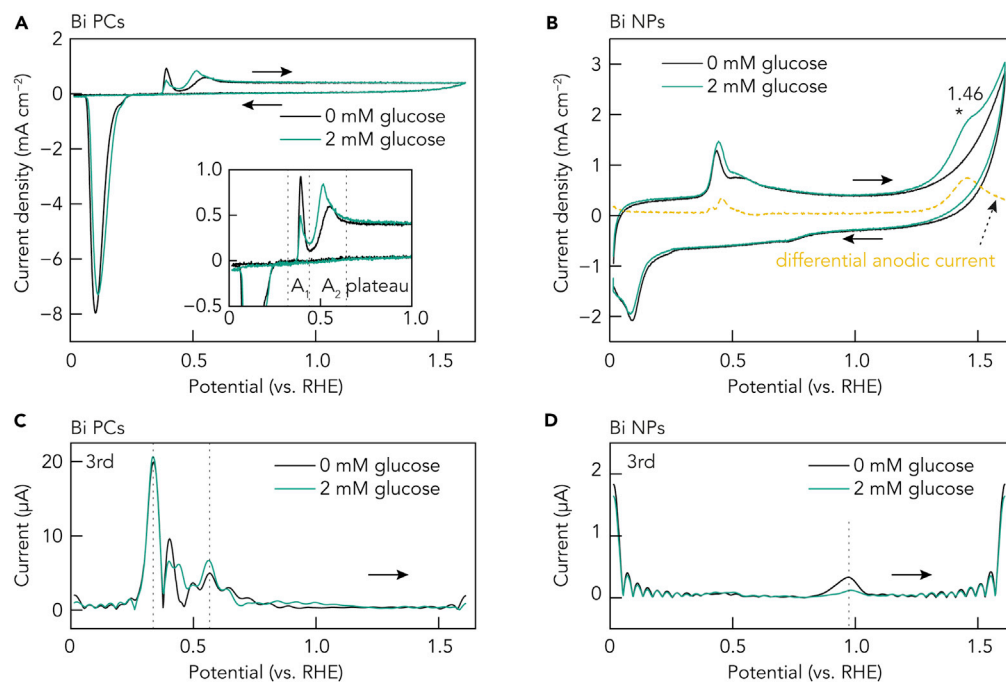
Figure 3. Electrochemistry of Bi PCs and NPs in 0.1 M KOH electrolyte with 2 mM glucose

(A and B) Comparison of CV plots between (A) Bi PCs and (B) Bi NPs/AC with/without 2 mM glucose. The scan rate is 5 mV s^{-1}. Inset of (A) shows the enlarged oxidation peaks from 0 to 1.0 V.

(C and D) The third harmonic components of the FTACV plots of (C) Bi PCs and (D) Bi NPs/AC during the anodic scan with/without 2 mM glucose in the electrolyte.

Figures 3C and 3D present the anodic FTACV profiles of both materials with/without 2 mM glucose. Bi PCs show no significant changes, whereas the rate of Bi(III) to Bi(V) electrooxidation of Bi NPs is slowed down (smaller FTACV current) after the addition of glucose. Based on the glucose electrooxidation mechanism on multi-valent transition metals (such as Cu, Ni) (Zheng et al., 2019b), a possible explanation is offered:

$$\text{Without glucose: Bi(III)} \xrightarrow{-2e^-} \text{Bi(V)} \xrightarrow{OH^-} \text{Bi(III)}$$

$$\text{With glucose: Bi(III)} - \text{glucose} \xrightarrow{-2e^-} \text{Bi(V)} - \text{glucose} \xrightarrow{redox} \text{Bi(III)} + \text{product(s)}$$

In the glucose-free electrolyte, after the Bi(III) oxidation to Bi(V), the high-valent species is unstable and would be converted to Bi(III) via a redox reaction. However, in the presence of glucose, the regeneration of Bi(III) species is kinetically controlled by the slower Bi(V)-glucose redox reaction (as well as glucose diffusion), resulting in a decreased high harmonic signal.

Why are BiPCs inactive for glucose electrooxidation?

Although the proposed mechanism on the Bi NPs is similar to that of transition metals, the significant difference between them is that bulk Bi (Bi PCs) shows no observable activity. The direct reason is that the Bi(V) species cannot be produced on the surface of Bi PCs at the same potential as that of the Bi NPs. However, the question still remains: why the enlargement of Bi particle size inhibits the production of Bi(V)?

To address this, we employed time-dependent electrochemical impedance spectroscopy (EIS) and analyzed the charge transfer resistance of both samples. Figure 4A illustrates the methodology where the electrodes were held at a pretreatment potential for different times before being subjected to the EIS test at OCP. Two pretreatment potentials at 0.4 and 1.0 V were selected to represent two scenarios for the Bi PCs: (1) the limited oxidation of the surface Bi(0) atoms and (2) the ready accumulation of Bi(III) oxide layers in the crystal, whereas for Bi NPs, both scenarios represent the full oxidation of Bi(0) to Bi(III).
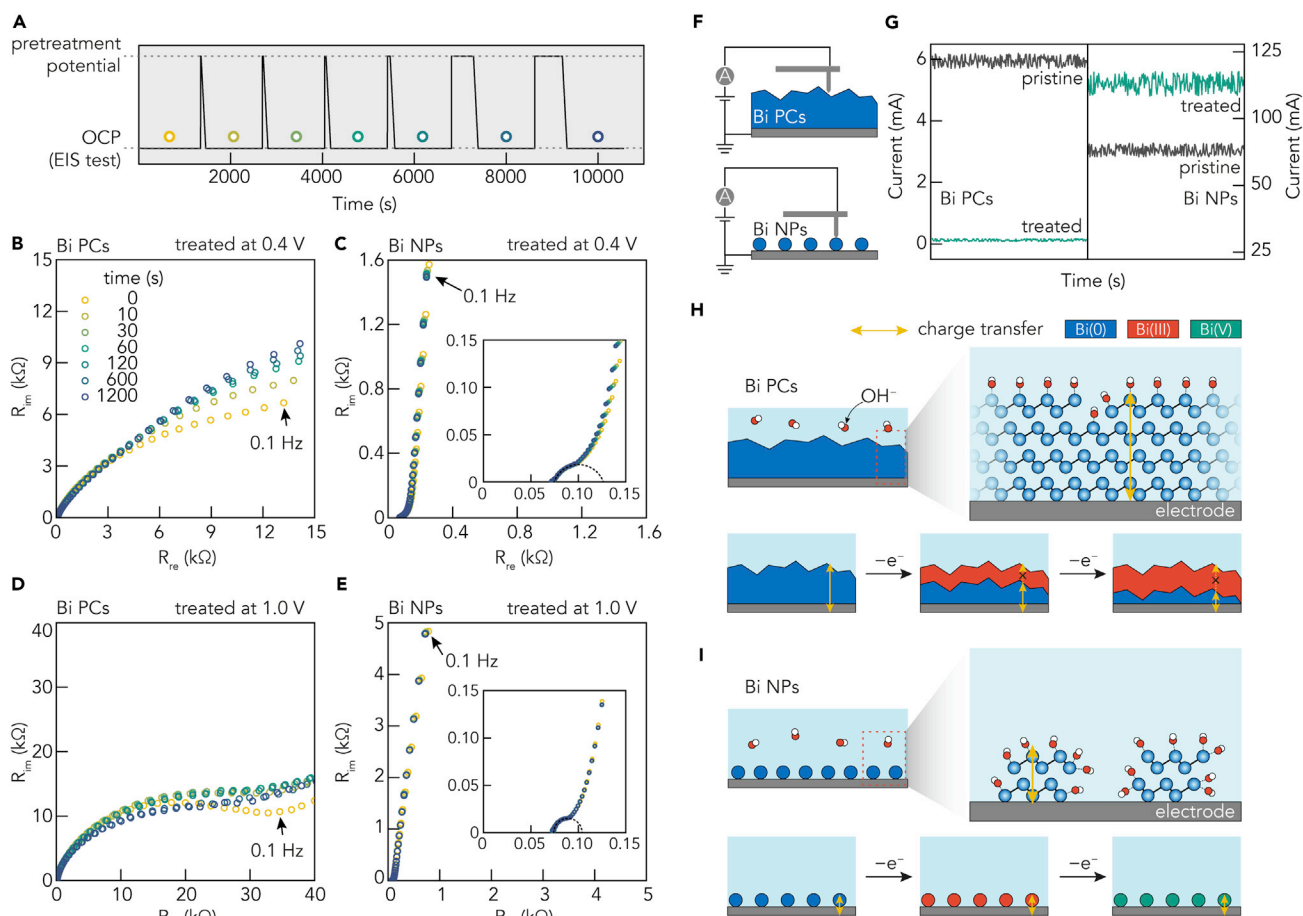
Figure 4. Resistance analysis of Bi PCs and Bi NPs at different oxidation states

(A) The potential sequence used for EIS testing. The electrode was held at pretreatment potential (0.4 and 1.0 V) for different durations before EIS testing at OCP.

(B–E) Nyquist plots of (B) Bi PCs pretreated at 0.4 V, (C) Bi NPs/AC pretreated at 0.4 V, (D) Bi PCs pretreated at 1.0 V, and (E) Bi NPs/AC pretreated at 1.0 V. Insets of (C and D) show the high-frequency domain with the semicircle outlined.

(F and G) C-AFM setup illustration and current profiles of Bi PCs and NPs in pristine and treated (1.0 V 1200 s) conditions.

(H and I) Illustration of the different electrooxidation behaviors of (H) Bi PCs and (I) NPs. For clarity, the activated carbon support of the Bi NPs is omitted. Yellow arrows indicate the simplified charge transfer path.

When treated at 0.4 V, the EIS spectra of Bi PCs (Figure 4B) are semicircular in shape, and their diameter represents the charge transfer resistance if a simple Randles circuit model is adopted. The charge transfer resistance increases as the amperometric treatment time prolongs, conforming to the thickening $Bi(OH)_3$ layer. On the contrary, the EIS spectra of the Bi NPs (Figure 4C) remain stable throughout the 1,200-s treatment, featuring a semicircle at high frequency and a diffusion line at the middle to low frequency. Remarkably, the charge transfer resistance of the Bi NPs is much smaller than that of the Bi PCs (97 Ω compared with 34 kΩ after 1,200-s treatment). Also, at the same frequency (0.1 Hz, for example), the resistance to transfer electrons in the Bi PCs is much higher than that of the Bi NPs.

As the treatment potential increases to 1.0 V, it is understood that the same $Bi(OH)_3$ layer in the Bi PCs can evolve faster. Therefore, higher resistance is expected. Figure 4D indeed shows the similar traits of the semicircle, but with much higher charge transfer resistance (45 kΩ at 1.0 V compared with 34 kΩ at 0.4 V after 1,200 s). However, the Bi NPs show a different trend, as Figure 4E suggests a smaller charge transfer resistance (68 Ω) than the treatment at 0.4 V (97 Ω). One possible reason is that the formation of Bi(V) species can assist charge transfer better than the insulating Bi(III) compounds ($Bi(OH)_3$ and Bi_2O_3).

Another direct evidence confirming the conductivity change is provided by conductive-AFM (C-AFM), as shown in Figures 4F (setup) and 4G (50 s current response). A voltage bias of 500 mV was applied between the cantilever and sample substance. The current signal before and after electrooxidation treatment (1.0 V versus RHE for 1,200 s) is presented as pristine and treated, respectively. Compared with its pristine form, the treated Bi PCs exhibit a much smaller current, suggesting the formation of an insulating layer on its surface. On the contrary, in agreement with the EIS results, the Bi NPs present an increased current signal after treatment, showing an accelerated charge transfer.

In brief, the different electrochemical behaviors of the Bi PCs and NPs are illustrated in Figures 4H and 4I. The Bi PCs-coated electrode features multi-layer Bi atoms, where the oxidation occurs sequentially from the surface to the bulk to form Bi(III) hydro(oxide) layers. Such layers possess high resistance, hindering the charge transfer between electrode and surface, and obstructing the diffusion of OH^- species to inner Bi sites. As a result, further oxidation of Bi(III) to Bi(V) is difficult. The Bi NPs-coated electrode does not have these problems. As the crystalline size of the Bi NPs is much smaller than that of PCs, the charge transfer path from the electrode to the NP's surface is significantly shorter. Even with the formation of $Bi(OH)_3$, the total resistance is much smaller due to the limited particle scale. Meanwhile, unlike the Bi PCs, the OH^- species can access Bi atoms on the NPs from all available coordination sites, meaning there is no diffusion limitation. As a result, the surface Bi(III) species can be oxidized to Bi(V) species to enable glucose oxidation.

Glucose electrooxidation on Bi NPs

To understand the glucose electrooxidation mechanism on the Bi NPs, we first studied the oxidation current response of various hydrocarbons containing C–OH structure. As shown in Figure 5A, compounds containing C(OH)–C(OH)–C(OH) structural fragment, such as glucose, glycerol, and gluconic acid, cause immediate current response once they are added to the electrolyte. In contrast, both ethanol and ethylene glycol show no current response. Therefore, the Bi NPs can selectively oxidize the C(OH)–C(OH)–C(OH) structure. Such selectivity is probably due to the difficulty of forming $C–O^-–Bi$ (hydrocarbon adsorbed on Bi surface) structure. Notably, the high selectivity to glycerol over ethylene glycol implies possible multi-site adsorption of hydrocarbon on Bi surface (three sites instead of two sites), which is of great importance to selective biomass conversion of glycerol. However, the electrooxidation of glycerol is beyond our scope of discussion here.

Knowing the structure of electrolysis products is essential for mechanism analysis. We performed a 3-h electrolysis of 1 mM glucose in 0.1 M KOH electrolyte with an applied potential of 1.47 V versus RHE using an H-type electrochemical cell. The possible leakage of Bi species from the electrode into the electrolyte is examined by inductive-coupled plasma optical emission spectrometry (ICP-OES). The results (see Table S1) indicate only trace amount of Bi (0.01–0.03 ppm) detected in the electrolyte, confirming that most of the Bi NPs remain on the electrode surface.

With a sampling interval of 30 min, the electrolyte is analyzed using an ultra-performance liquid chromatography-tandem mass spectrometer (UPLC-MS/MS) (see transparent methods for analytical details). Figures 5B and 5C show the corresponding current response and product analysis. The initial stage (0–30 min) shows the highest reaction rate (current), and a steady oxidation current of $ca.$ 0.4 mA cm^{-2} is presented after 1 h. Interestingly, the UPLC-MS/MS analyses (see Figure S7 and S8, and Table S2 for data) reveal four products, gluconic acid, arabinonic acid, erythronic acid, and glyceric acid, with decreasing carbon atom numbers of 6, 5, 4, and 3. The time-dependent product distribution results in Figure 5C show that glucose is significantly consumed within 30 min with gluconic acid as the main product. However, further electrolysis causes decreasing gluconic acid concentration and increasing C5 (arabinonic acid), C4 (erythronic acid), and C3 (glyceric acid) products. After 3 h, glyceric acid is the dominating product, followed by C4 and C5 products, whereas the C6 product (gluconic acid) is minor. The structure of the Bi NPs before and after electrocatalysis is compared in Figure S3. Apart from producing some larger particles, likely due to aggregation, no significant size change of most Bi NPs is found. These results, together with the ICP-OES analysis, demonstrate the high stability of Bi NPs during electrooxidation.

The UPLC-MS/MS results suggest that the Bi NPs can perform C–C bond cleavage selectively. It is currently widely accepted in the literature that the product of glucose electrooxidation is gluconic acid regardless of the electrocatalyst (Au, Pt, Ni, Cu, etc.) (Brouzgou and Tsiakaras, 2015). However, our data suggest an extended route that shows gluconic acid is not the final product. Figure 5A confirms that gluconic acid can be oxidized at the same condition as glucose. The decreasing concentration of gluconic acid after 1 h (Figure 5A) also
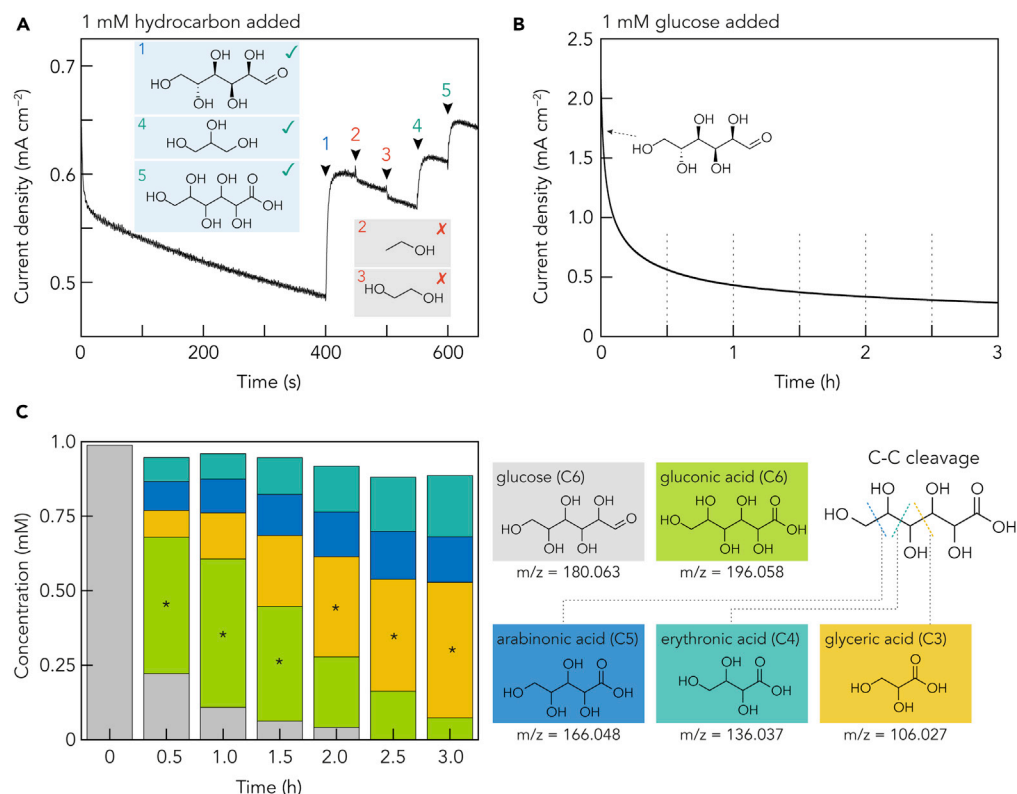
Figure 5. Mechanism study of glucose electrooxidation on Bi NPs

(A) Amperometric response of Bi NPs/AC (Bi: 1.5 wt %)-coated GCE to various hydrocarbon compounds: 1: glucose, 2: ethanol, 3: ethylene glycol, 4: glycerol, and 5: gluconic acid. The hydrocarbon concentration in 0.1 M KOH electrolyte is 1 mM, and the applied potential is 1.47 V versus RHE.

(B) Long-term (3 h) electrolysis of 1 mM glucose in 0.1 M KOH electrolyte using Bi NPs/AC (Bi: 1.5 wt %)-coated carbon paper electrode. Applied potential is 1.47 V versus RHE.

(C) Product analysis results from UPLC-MS/MS at different times during the long-term electrolysis. The main product is marked with *.

suggests that gluconic acid is an intermediate and can be further oxidized to C5, C4, and C3 products. A detailed comparison between the Bi and other metal electrocatalysts is summarized in Table S3.

Therefore, we propose a mechanism of Bi NPs-catalyzed glucose electrooxidation in Scheme 2. Two main routes are involved, namely, the glucose to gluconic acid oxidation and the following C–C bond cleavage to produce C5, C4, and C3 compounds. First, the glucose molecule is adsorbed on the Bi(III)–OH surface to form a C–O–Bi(III) bond. With the oxidization of Bi(III) to Bi(V), the adsorbed glucose molecule tends to donate electrons to the Bi(V) sites and to be oxidized to gluconolactone, followed by hydrolysis to gluconic acid. This process is similar to other multivalent electrocatalysts, such as Cu (Zheng et al., 2017) and Au (Juřík et al., 2016). Second, the produced gluconic acid molecules are also adsorbed on the Bi(V) surface, most likely via multiple Bi(V) sites. The highly oxidizing Bi(V) species then draw electrons from the carbon atoms, weakening the C–C bonding, and eventually breaking it to produce C5, C4, and C3 compounds.

After understanding the mechanism of glucose oxidation, we further evaluated the electrocatalytic activity of the Bi NPs. Quantitative analysis was performed by changing the catalyst loading and glucose concentration, and the results are summarized in Figure 6. As suggested in Figures 6A and 6B, an optimal catalyst loading of 40 μg is evident as a lower or higher mass loading would produce a lower oxidation peak current. Understandably, compared with 20 μg, a higher catalyst loading of 40 μg provides more charge transfer sites. Nevertheless, excessive coating would increase the diffusion path of glucose molecules, which in turn would lower the peak current.
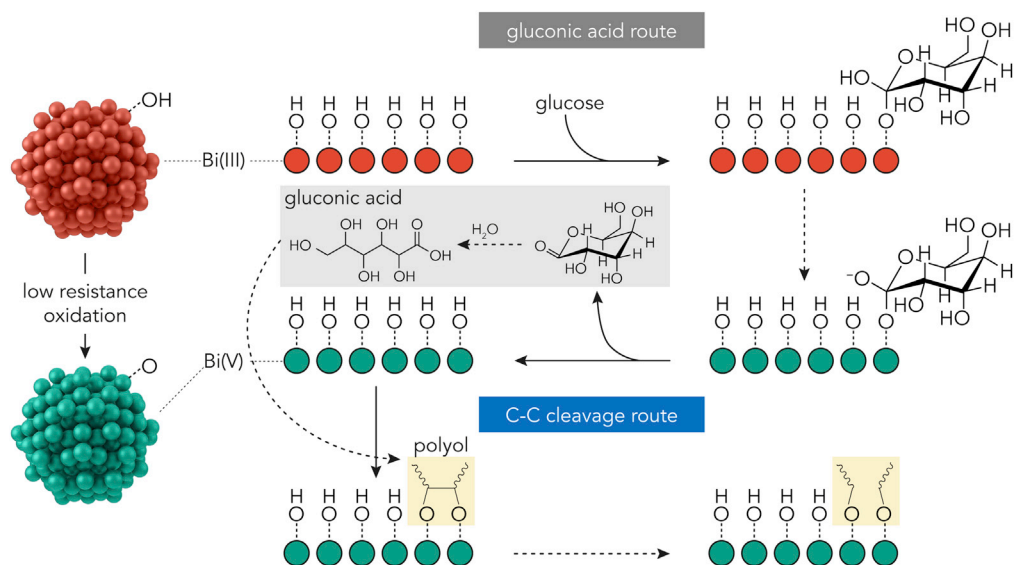
Scheme 2. Proposed continuous glucose electrooxidation mechanism on Bi NPs electrocatalyst

Varying the reaction temperature can provide insights into the reaction activation parameters. As shown in Figures 6C and 6D, higher temperature (from 25°C to 45°C) causes higher oxidation current (reaction rate). Moreover, the oxidation peak potential decreases slightly (2.4 mV °C^{-1}), which is due to the accelerated glucose diffusion at a higher temperature. However, because the mechanism involves more than one step and the transferred electron number is difficult to assume, the activation energy of overall glucose electrooxidation on Bi NPs cannot be calculated accurately.

Finally, we studied the impact of glucose concentration on the corresponding oxidation signal (Figures 6E and 6F). Increasing the glucose concentration would promote oxidation signal, confirming that the peak at 1.46 V can be exclusively attributed to glucose electrooxidation on the Bi NPs catalyst. A well-fitted (R = 0.98) linear relationship between the oxidation current density and glucose concentration is presented with a slope of 582 μA mM^{-1} cm^{-2}. This excellent correlation implies the potential application of the Bi NPs as an electrochemical glucose sensor. With a sensitivity of 582 μA mM^{-1} cm^{-2}, the performance of the Bi NPs is comparable to those of some state-of-the-art transition metal catalysts (Zheng et al., 2019a).

Conclusion

In summary, we prepared stabilizer-free Bi NPs with a mean diameter of 9.6 nm using a laser ablation method. The electrochemical properties and glucose electrooxidation activity of the Bi PCs and Bi NPs in alkaline conditions are compared using CV and FTACV. It is found that the Bi NPs can generate Bi(V) species on its surface at high anodic potential and act as the electrocatalyst for glucose electrooxidation, whereas the BiPCs cannot. Evidence from both EIS and C-AFM suggests that the formation of a non-conductive Bi(OH)$_3$ layer on the Bi PCs surface during anodic polarization prevents further electrooxidation of Bi(III) to Bi(V), whereas the much shorter charge transfer pathway of the Bi NPs significantly reduces the impact of Bi(OH)$_3$ layer formation, enabling high-valent Bi(V) species production, which also benefits the charge transfer.

The formation of Bi(V) species on the surface of the Bi NPs is the reason for its glucose electrooxidation activity. Contrary to common belief that gluconic acid is the final product, glucose electrooxidation catalyzed by the Bi NPs produces gluconic acid as the intermediate product, which can be further oxidized to C5 (arabinonic acid), C4 (erythronic acid), and C3 (glyceric acid) products during long-term electrolysis. A highly selective glucose oxidation mechanism involving C–C bond cleavage is thus suggested. Also, the Bi NPs, but not ethylene glycol, show selective catalytic activity toward glycerol electrooxidation, suggesting a possible multi-Bi(V) site adsorption mechanism.

These results represent one of the first examples of using Bi-only electrocatalyst for electrooxidation. We not only explain why Bi PCs do not show any catalytic activity but also present a method to prepare Bi NPs
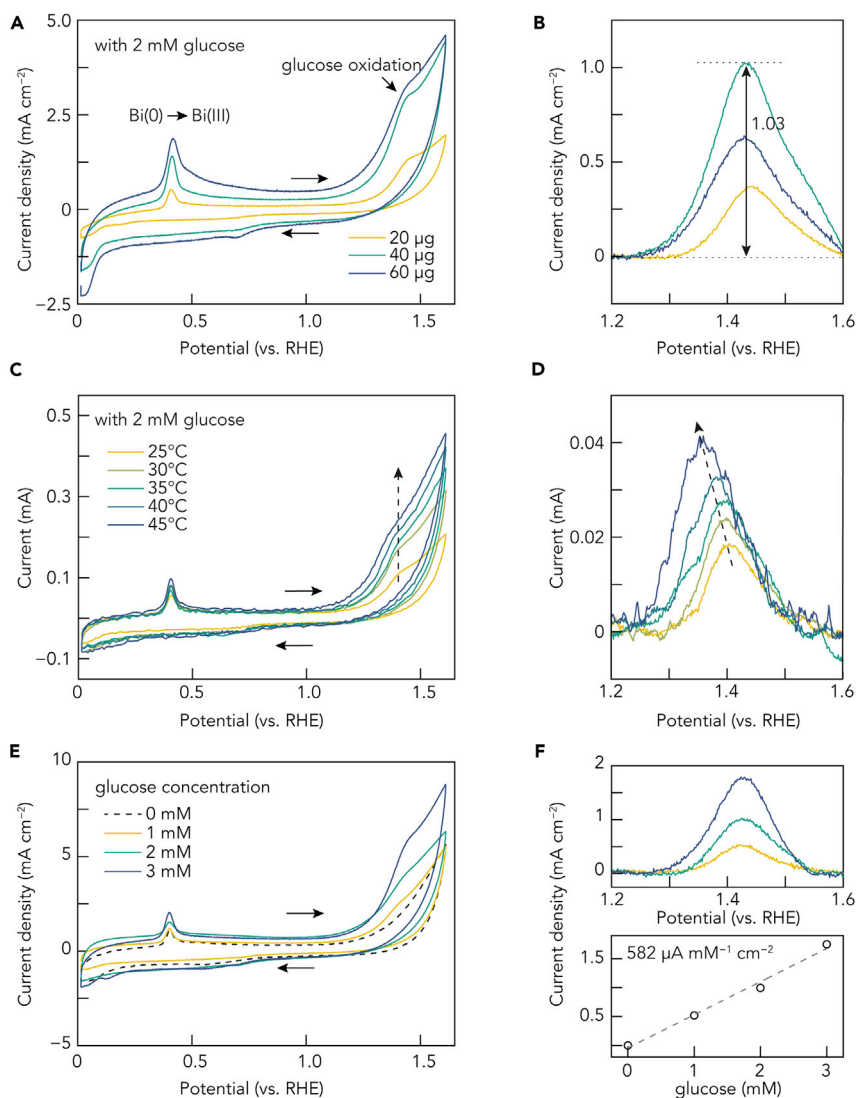
Figure 6. Quantitative analysis of glucose electrooxidation on Bi NPs

(A) CV plots of electrodes coated with different amounts (20, 40, and 60 μg) of the Bi NPs/AC (Bi: 1.5 wt %) composites in 0.1 M KOH electrolyte with 2 mM glucose.

(B) Corresponding glucose electrooxidation signal in (A) after background subtraction.

(C) CV plots of the Bi NPs/AC-coated (40 μg) electrode in 0.1 M KOH electrolyte with 2 mM glucose at different temperatures.

(D) Corresponding glucose electrooxidation signal in (C) after background subtraction.

(E) CV plots of the Bi NPs/AC-coated (40 μg) electrode in 0.1 M KOH electrolyte with different glucose concentrations (0, 1, 2, and 3 mM).

(F) Corresponding glucose electrooxidation signal in (E) after background subtraction (up) and the linear correlation between oxidation peak current density and glucose concentration (down).

electrocatalyst suitable for oxidation applications, which is of great importance especially for bioelectrocatalysis in which the less toxic bismuth is highly appreciated. Moreover, the high selectivity and ability to break C–C bond make Bi NPs a promising catalyst for electrochemical biomass conversion and organic synthesis.

Limitations of the study

Our work demonstrates the electrocatalytic activity of Bi NPs for polyol (mainly glucose) electrooxidation and suggests that the C–C bond cleavage is promoted via the formation of the surface Bi(V) species. We

also explain why Bi PCs are not active using mainly electrochemical data. However, a deeper understanding of the Bi surface during the anodic catalysis is still required. It is only possible by engaging *in situ* techniques coupled with electrochemistry, such as Raman and XRD. Furthermore, the impact of particle morphology (shape and size) on the electrocatalytic activity and selectivity needs to be further investigated. This requires the shape/size-controllable synthesis of Bi NPs, which we are currently working on.

Resource availability

Lead contact

Further information and requests for resources should be directed to and will be fulfilled by the lead contact, Lawrence Yoon Suk Lee (lawrence.ys.lee@polyu.edu.hk).

Materials availability

This study did not generate new reagents.

Data and code availability

This article includes all datasets/code generated or analyzed during this study.

METHODS

All methods can be found in the accompanying Transparent Methods supplemental file.

SUPPLEMENTAL INFORMATION

Supplemental information can be found online at https://doi.org/10.1016/j.isci.2021.102342.

AUTHOR CONTRIBUTIONS

W.Z. and L.Y.S.L conceived the original idea. W.Z. designed the experiments, conducted the material synthesis, and CV, FTACV, EIS, AFM, and C-AFM experiments. Y.L. performed the XRD, TEM, and *i*-t testing. C.-S.T. and P.-K.S. carried out the UPLC-MS/MS analysis. L.Y.S.L. supervised the progress of this project and drafted the manuscript with W.Z.

DECLARATION OF INTERESTS

The authors declare no competing interests.

REFERENCES

Amendola, V., and Meneghetti, M. (2009). Laser ablation synthesis in solution and size manipulation of noble metal nanoparticles. Phys. Chem. Chem. Phys. *11*, 3805–3821.

Betsch, R.J., and White, W.B. (1978). Vibrational spectra of bismuth oxide and the sillenite-structure bismuth oxide derivatives. Spectrochim. Acta A *34*, 505–514.

Brouzgou, A., and Tsiakaras, P. (2015). Electrocatalysts for glucose electrooxidation reaction: a review. Top. Catal. *58*, 1311–1327.

Cereceda-Company, P., and Costa-Kramer, J.L. (2018). Electrochemical growth of bismuth for X-ray absorbers. J. Electrochem. Soc. *165*, D167–D182.

Chen, T., Liu, D., Lu, W., Wang, K., Du, G., Asiri, A.M., and Sun, X. (2016). Three-dimensional Ni$_2$P nanoarray: an efficient catalyst electrode for sensitive and selective nonenzymatic glucose sensing with high specificity. Anal. Chem. *88*, 7885–7889.

de Souza, M.B.C., Vicente, R.A., Yukuhiro, V.Y., Pires, V.M.T., C.T.G., Cheuquepán, W., Bott-

Neto, J.L., Solla-Gullón, J., and Fernández, P.S. (2019). Bi-modified Pt electrodes toward glycerol electrooxidation in alkaline solution: effects on activity and selectivity. ACS Catal. *9*, 5104–5110.

de Souza, M.B.C., Yukuhiro, V.Y., Vicente, R.A., Vilela Menegaz Teixeira Pires, C.T.G., Bott-Neto, J.L., and Fernández, P.S. (2020). Pb- and Bi-modified Pt electrodes toward glycerol electrooxidation in alkaline media. Activity, selectivity, and the importance of the Pt atoms arrangement. ACS Catal. *10*, 2131–2137.

Deng, P., Wang, H., Qi, R., Zhu, J., Chen, S., Yang, F., Zhou, L., Qi, K., Liu, H., and Xia, B.Y. (2019). Bismuth oxides with enhanced bismuth–oxygen structure for efficient electrochemical reduction of carbon dioxide to formate. ACS Catal. *10*, 743–750.

Espinosa, A.M., San José, M.T., Tascón, M.L., Vászquez, M.D., and Sánchez Batanero, P. (1991). Electrochemical behaviour of bismuth(V) and bismuth(III) compounds at a carbon paste electrode. Application to the study of the superconductor BiSrCaCuO. Electrochim. Acta *36*, 1561–1571.

Garcia, A.C., Birdja, Y.Y., Tremiliosi-Filho, G., and Koper, M.T.M. (2017). Glycerol electro-oxidation on bismuth-modified platinum single crystals. J. Catal. *346*, 117–124.

Gong, Q., Ding, P., Xu, M., Zhu, X., Wang, M., Deng, J., Ma, Q., Han, N., Zhu, Y., Lu, J., et al. (2019). Structural defects on converted bismuth oxide nanotubes enable highly active electrocatalysis of carbon dioxide reduction. Nat. Commun. *10*, 2807.

Heller, A., and Feldman, B. (2008). Electrochemical glucose sensors and their applications in diabetes management. Chem. Rev. *108*, 2482–2505.

Heuer-Jungemann, A., Feliu, N., Bakaimi, I., Hamaly, M., Alkilany, A., Chakraborty, I., Masood, A., Casula, M.F., Kostopoulou, A., Oh, E., et al. (2019). The role of ligands in the chemical synthesis and applications of inorganic nanoparticles. Chem. Rev. *119*, 4819–4880.

Juřík, T., Podešva, P., Farka, Z., Kováľ, D., Skládal, P., and Foret, F. (2016). Nanostructured gold deposited in gelatin template applied for electrochemical assay of glucose in serum. Electrochim. Acta *188*, 277–285.

Kanatzidis, M., Sun, H., and Dehnen, S. (2020). Bismuth-the magic element. Inorg. Chem. *59*, 3341–3343.

Li, F., Gu, G.H., Choi, C., Kolla, P., Hong, S., Wu, T.-S., Soo, Y.-L., Masa, J., Mukerjee, S., Jung, Y., et al. (2020). Highly stable two-dimensional bismuth metal-organic frameworks for efficient electrochemical reduction of CO2. Appl. Catal. B *277*, 119241.

Li, L.Q., Tang, C., Xia, B.Q., Jin, H.Y., Zheng, Y., and Qiao, S.Z. (2019). Two-dimensional mosaic bismuth nanosheets for highly selective ambient electrocatalytic nitrogen reduction. ACS Catal. *9*, 2902–2908.

Madhura, T.R., Gnana Kumar, G., and Ramaraj, R. (2020). Reduced graphene oxide-supported Co₃O₄ nanocomposite bifunctional electrocatalysts for glucose–oxygen fuel cells. Energy Fuels *34*, 12984–12994.

Medina-Ramos, J., Lee, S.S., Fister, T.T., Hubaud, A.A., Sacci, R.L., Mullins, D.R., DiMeglio, J.L., Pupillo, R.C., Velardo, S.M., Lutterman, D.A., et al. (2017). Structural dynamics and evolution of bismuth electrodes during electrochemical reduction of CO₂ in imidazolium-based ionic liquid solutions. ACS Catal. *7*, 7285–7295.

Nordberg;, G.F., Fowler, B.A., and Nordberg, M. (2015). Handbook on the Toxicology of Metals, 4th edn (Elsevier).

Phan, C.M., and Nguyen, H.M. (2017). Role of capping agent in wet synthesis of nanoparticles. J. Phys. Chem. A *121*, 3213–3219.

Planas, O., Wang, F., Leutzsch, M., and Cornella, J. (2020). Fluorination of arylboronic esters enabled by bismuth redox catalysis. Science *367*, 313–317.

Pourbaix, M. (1974). Atlas of Electrochemical Equilibria in Aqueous Solutions (National Association of Corrosion)).

Sandnes, E., Williams, M.E., Bertocci, U., Vaudin, M.D., and Stafford, G.R. (2007). Electrodeposition of bismuth from nitric acid electrolyte. Electrochim. Acta *52*, 6221–6228.

Vila, M., Díaz-Guerra, C., and Piqueras, J. (2012). Luminescence and Raman study of α-Bi₂O₃ ceramics. Mater. Chem. Phys. *133*, 559–564.

Vivier, V., Cachet-Vivier, C., Mezaille, S., Wu, B.L., Cha, C.S., Nedelec, J.Y., Fedoroff, M., Michel, D., and Yu, L.T. (2000). Electrochemical study of Bi₂O₃ and Bi₂O₂CO₃ by means of a cavity microelectrode. I. Observed phenomena and direct analysis of results. J. Electrochem. Soc. *147*, 4252–4262.

Vivier, V., Regis, A., Sagon, G., Nedelec, J.Y., Yu, L.T., and Cachet-Vivier, C. (2001). Cyclic voltammetry study of bismuth oxide Bi₂O₃ powder by means of a cavity microelectrode coupled with Raman microspectrometry. Electrochim. Acta *46*, 907–914.

Wang, Y., Shi, M.M., Bao, D., Meng, F.L., Zhang, Q., Zhou, Y.T., Liu, K.H., Zhang, Y., Wang, J.Z., Chen, Z.W., et al. (2019). Generating defect-rich bismuth for enhancing the rate of nitrogen electroreduction to ammonia. Angew. Chem. Int. Ed. *58*, 9464–9469.

Wei, Z., Dubceac, C., Petrukhina, M.A., and Dikarev, E.V. (2019). From a volatile molecular precursor to twin-free single crystals of bismuth. Chem. Commun. *55*, 5717–5719.

Wenkin, M., Ruiz, P., Delmon, B., and Devillers, M. (2002). The role of bismuth as promoter in Pd-Bi catalysts for the selective oxidation of glucose to gluconate. J. Mol. Catal. A Chem. *180*, 141–159.

Williams, D.E., and Wright, G.A. (1976). Nucleation and growth of anodic oxide films on bismuth—I. Cyclic voltammetry. Electrochim. Acta *21*, 1009–1019.

Williams, D.E., and Wright, G.A. (1977). Nucleation and growth of anodic oxide films on bismuth—II. Electrochim. Acta *22*, 505–508.

Wrona, P.K., and Galus, Z. (1980). Electrode processes of bismuth in weakly acidic, neutral and alkaline-solutions. Electrochim. Acta *25*, 419–428.

Xia, F., Xu, X., Li, X., Zhang, L., Zhang, L., Qiu, H., Wang, W., Liu, Y., and Gao, J. (2014). Preparation of bismuth nanoparticles in aqueous solution and its catalytic performance for the reduction of 4-nitrophenol. Ind. Eng. Chem. Res. *53*, 10576–10582.

Yao, D., Tang, C., Li, L., Xia, B., Vasileff, A., Jin, H., Zhang, Y., and Qiao, S.Z. (2020). In situ fragmented bismuth nanoparticles for electrocatalytic nitrogen reduction. Adv. Energy Mater. *10*, 2001289.

Yarema, M., Kovalenko, M.V., Hesser, G., Talapin, D.V., and Heiss, W. (2010). Highly monodisperse bismuth nanoparticles and their three-dimensional superlattices. J. Am. Chem. Soc. *132*, 15158–15159.

Zeng, H., Du, X.-W., Singh, S.C., Kulinich, S.A., Yang, S., He, J., and Cai, W. (2012). Nanomaterials via laser ablation/irradiation in liquid: a review. Adv. Funct. Mater. *22*, 1333–1353.

Zhang, E.H., Wang, T., Yu, K., Liu, J., Chen, W.X., Li, A., Rong, H.P., Lin, R., Ji, S.F., Zhene, X.S., et al. (2019). Bismuth single atoms resulting from transformation of metal-organic frameworks and their use as electrocatalysts for CO₂ reduction. J. Am. Chem. Soc. *141*, 16569–16573.

Zhang, Y., Simonov, A.N., Zhang, J., and Bond, A.M. (2018). Fourier transformed alternating current voltammetry in electromaterials research: direct visualisation of important underlying electron transfer processes. Curr. Opin. Electrochem. *10*, 72–81.

Zheng, W., Lee, J., Gao, Z.W., Li, Y., Lin, S., Lau, S.P., and Lee, L.Y.S. (2020). Laser-assisted ultrafast exfoliation of black phosphorus in liquid with tunable thickness for Li-ion batteries. Adv. Energy Mater. *10*, 1903490.

Zheng, W., Li, Y., Hu, L., and Lee, L.Y.S. (2019a). Use of carbon supports with copper ion as a highly sensitive non-enzymatic glucose sensor. Sens. Actuators, B *282*, 187–196.

Zheng, W., Li, Y., and Lee, L.Y.S. (2019b). Insights into the transition metal ion-mediated electrooxidation of glucose in alkaline electrolyte. Electrochim. Acta *308*, 9–19.

Zheng, W., Li, Y., Tsang, C.-S., Hu, L., Liu, M., Huang, B., Lee, L.Y.S., and Wong, K.-Y. (2017). CuII-mediated ultra-efficient electrooxidation of glucose. ChemElectroChem *4*, 2788–2792.

Supplemental information

Stabilizer-free bismuth nanoparticles

for selective polyol electrooxidation

Weiran Zheng, Yong Li, Chui-Shan Tsang, Pui-Kin So, and Lawrence Yoon Suk Lee

Figures
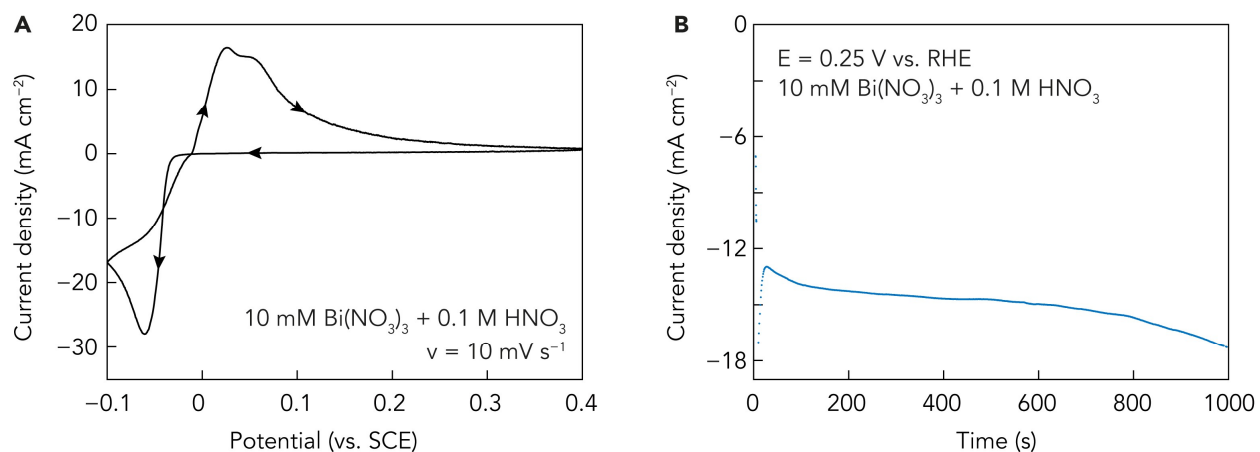
Figure S1. Electrochemical data related to the electrochemical deposition of Bi polycrystal on GCE, Related to Transparent Methods: Electrochemical deposition of Bi PCs, Related to Figure 1, sample preparation in main text, and Transparent Methods: Electrochemical deposition of Bi PCs

(A) CV plot of GCE in an aqueous electrolyte containing 10 mM $Bi(NO_3)_3$ and 0.1 M HNO_3.
(B) Current signal during the 1000 s constant-potential (E = 0.25 V $vs.$ RHE) deposition on GCE.
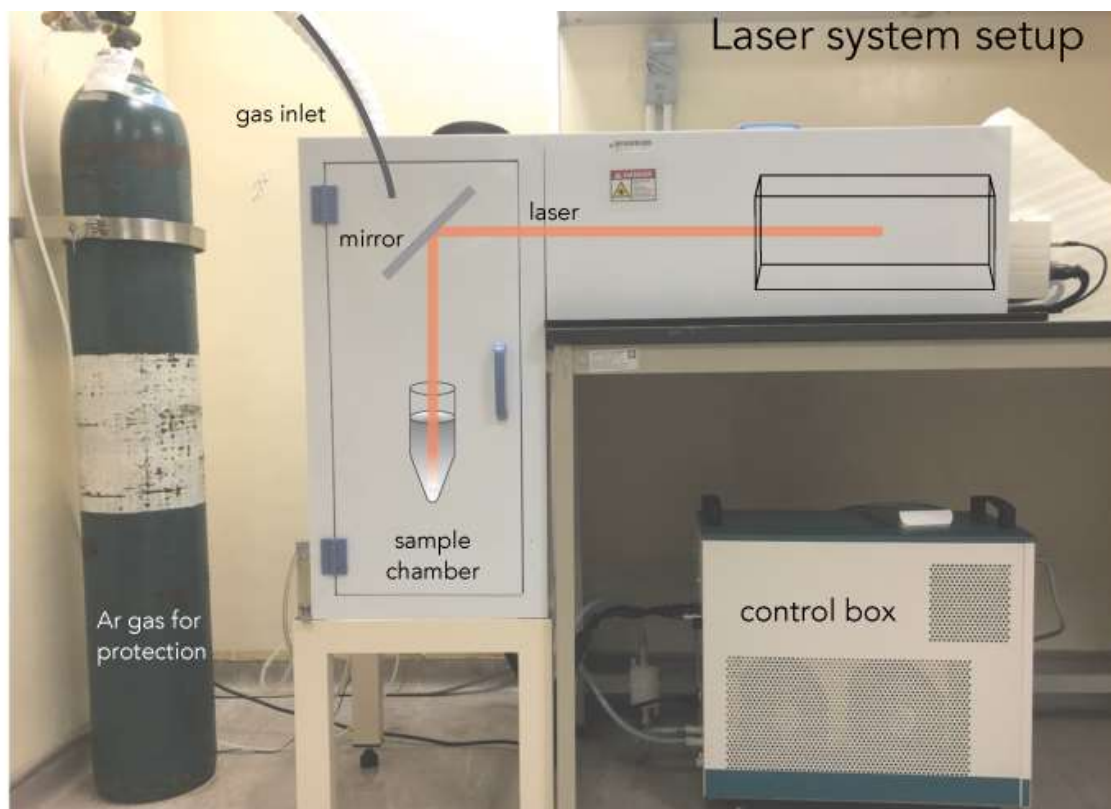
Figure S2. Experimental setup for laser ablation in liquid environment, Related to Scheme 1, Figure 1, and Transparent Methods: Laser ablation for Bi NPs production

The sample chamber was filled with Ar gas to avoid fire hazards.
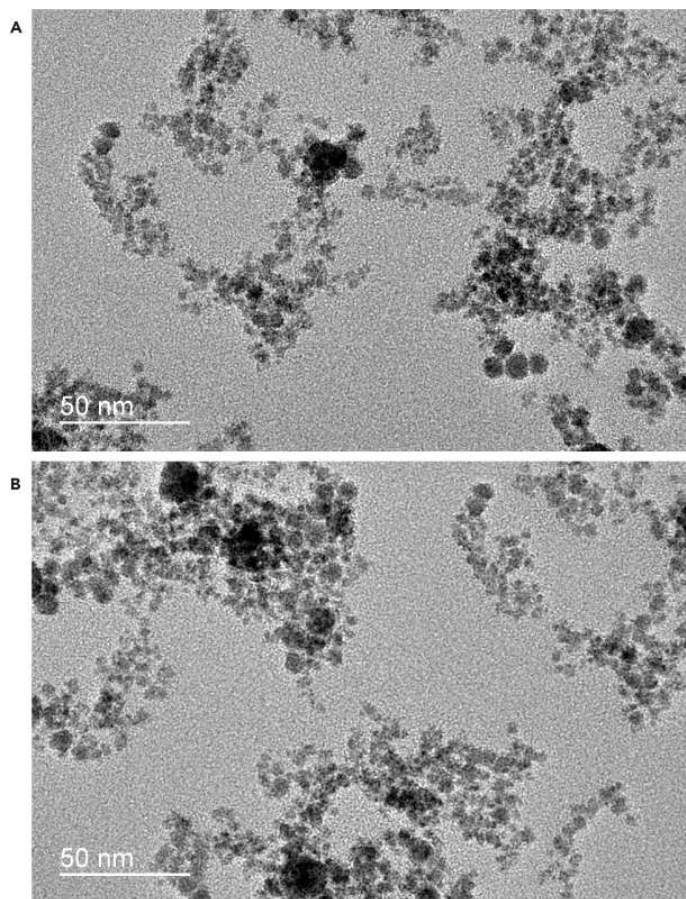
Figure S3. Low magnification TEM images of Bi NPs, Related to Figure 1
(A) Before electrolysis.
(B) After electrolysis (3 h) and reduced back to Bi^0 at E = 0.25 V *vs*. RHE for 5 min.
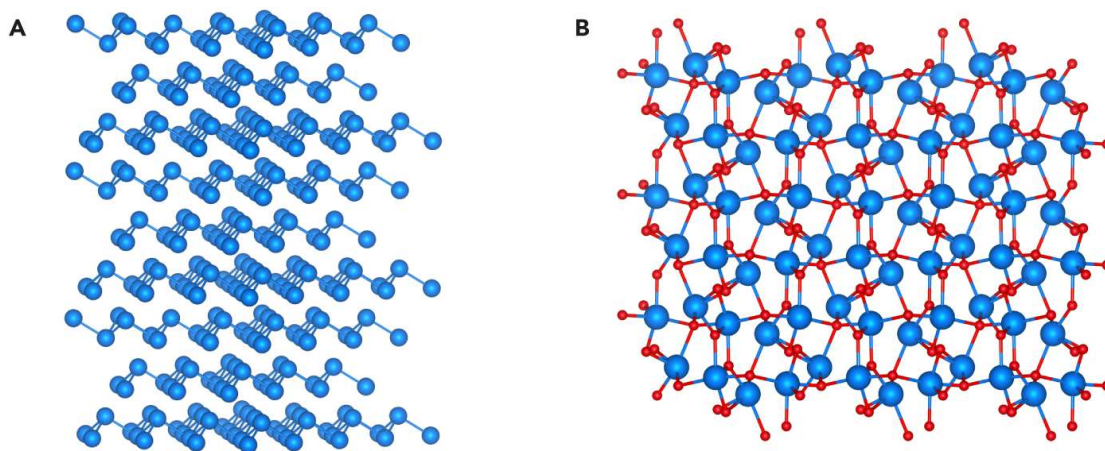
Figure S4. Structures of materials with cell size of 3×3×3, Related to Figure 2
Bi and O atoms are represented by blue and red balls, respectively. The unit cell parameters are collected from the Crystallography Open Database (COD): Bi(id: 7123351), alpha-Bi_2O_3(id: 1526458), and visualized using VESTA software.
(A) Bi.
(B) alpha-Bi_2O_3.
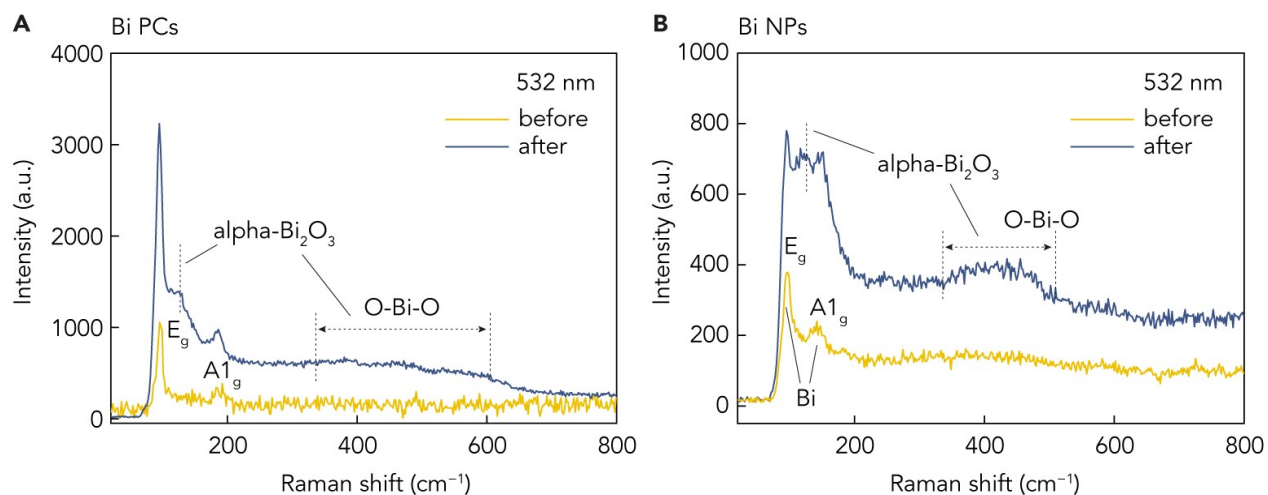
Figure S5. Raman spectra of modified electrodes before and after 1 h of electrooxidation at 0.8 V vs. RHE in 0.1 M KOH, Related to Figure 2
The laser wavelength is 532 nm, power is 5 mW.
(A) Bi PCs.
(B) Bi NPs.
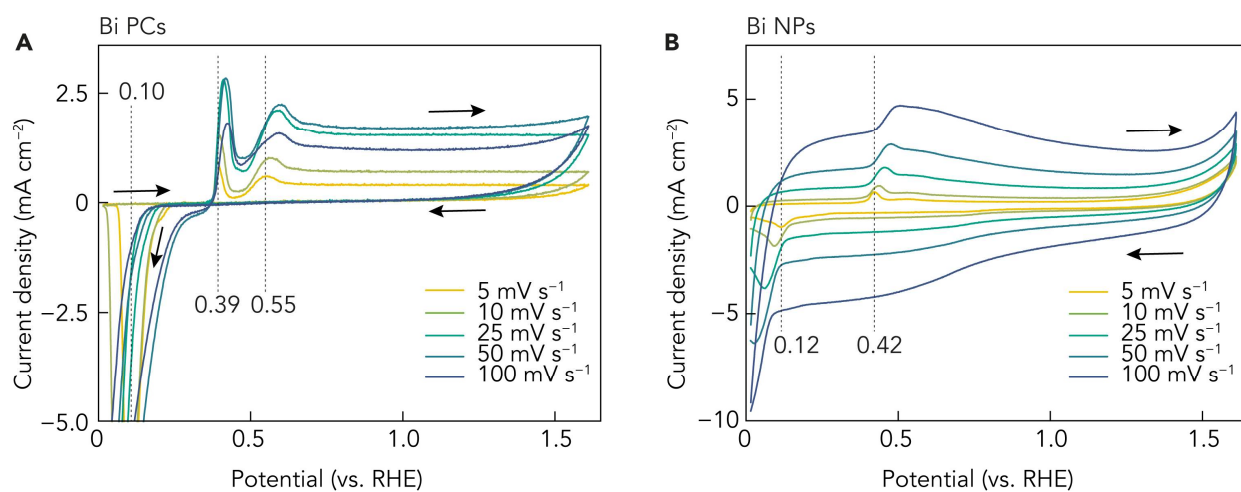
Figure S6. Scan rate dependent CV plots of modified electrodes in 0.1 M KOH electrolyte, Related to Figure 2
(A) Bi PCs.
(B) Bi NPs.

UPLC–MS/MS calibration

Glucose (r = 0.98488)
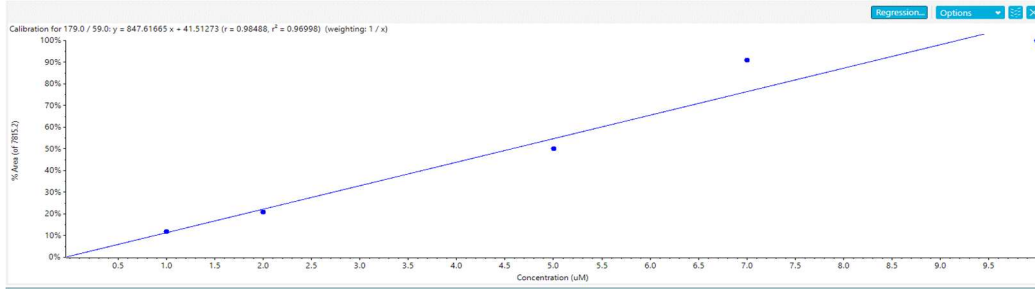
Gluconic acid (r = 0.99787)
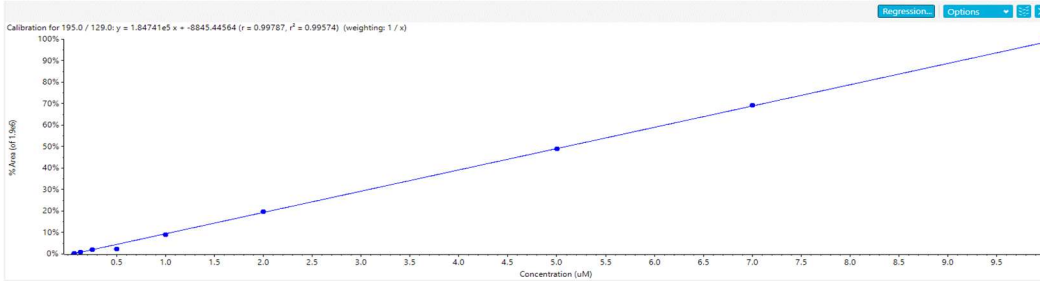
Arabinonic acid (r = 0.99802)
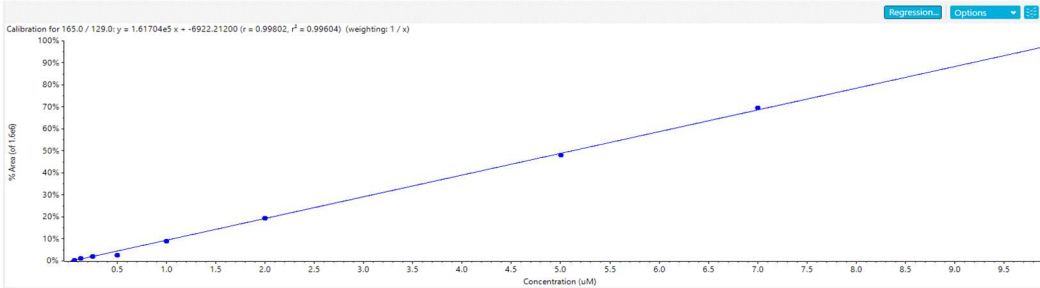
Erythronic acid (r = 0.99824)
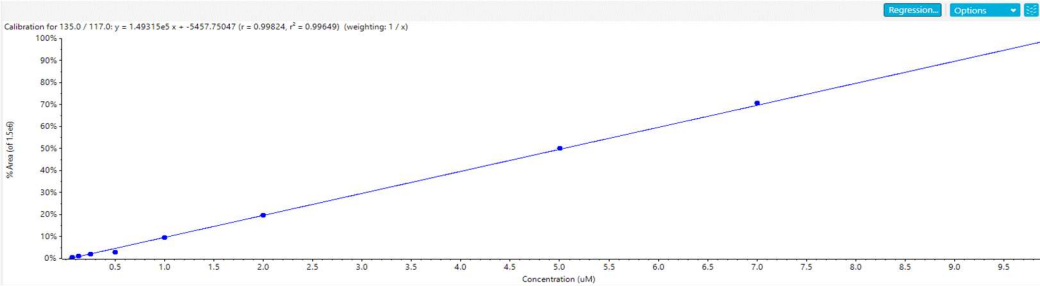
Glyceric acid (r = 0.99795)
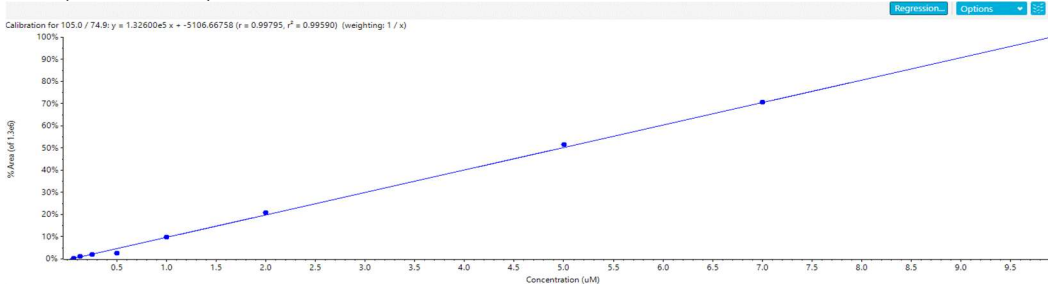
Figure S7. Calibration curves for all identified compounds, Related to Figure 5 and Transparent Methods

UPLC–MS/MS spectra of products

Glucose (0.810-0.893 min)

Mass	179.0555
Calc. mass	179.0561
mDa	0.61
Formula	C6H11O6 ([M-H]−)
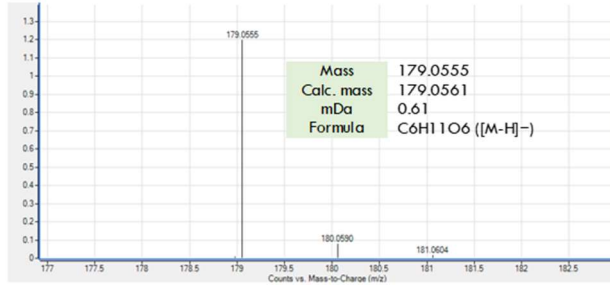
Glyceric acid (0.123-0.189 min)

Mass	105.0193
Calc. mass	105.0193
mDa	0.03
Formula	C3H5O4 ([M-H]−)
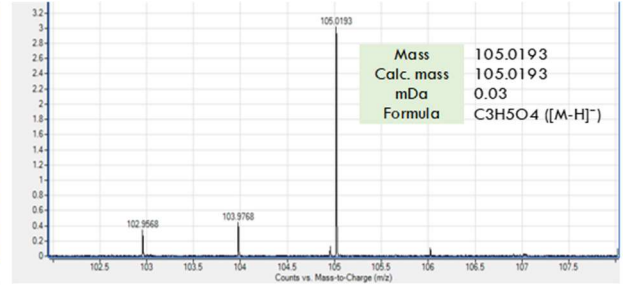
Gluconic acid (0.133-0.200 min)

Mass	195.0509
Calc. mass	195.051
mDa	0.13
Formula	C6H11O7 ([M-H]−)
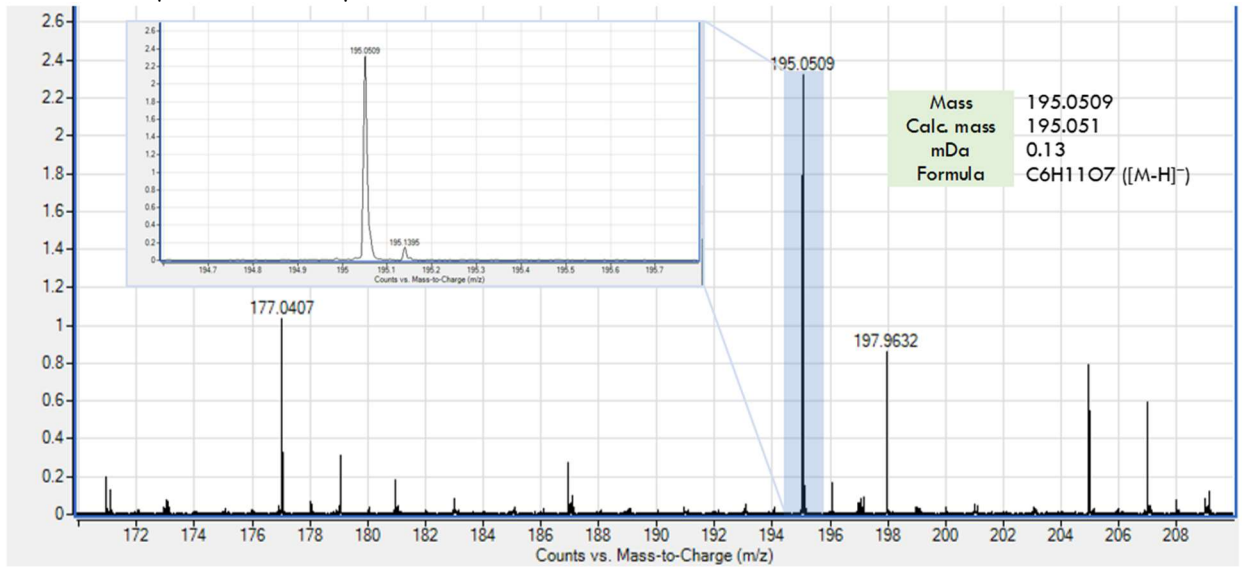
Arabinonic acid (0.126-0.160 min)

Mass	165.0409
Calc. mass	165.0405
mDa	0.44
Formula	C5H10O6 ([M-H]−)
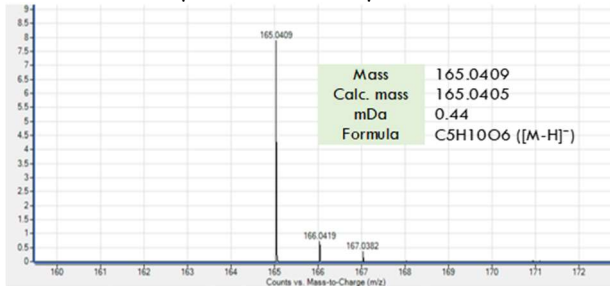
Erythronic acid (0.119-0.169 min)

Mass	135.03
Calc. mass	135.0299
mDa	0.1
Formula	C4H7O5 ([M-H]−)
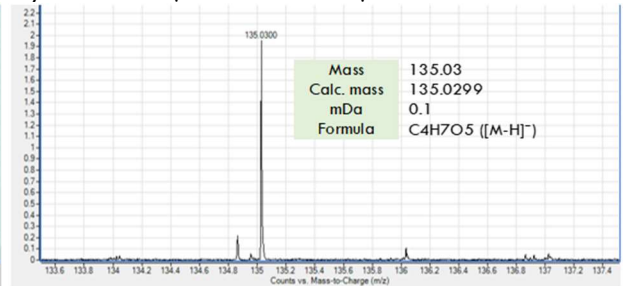
Figure S8. Mass spectra of products and their identification, Related to Figure 5 and Transparent Methods

Table S1. Inductive Coupled Plasma Optical Emission Spectrometer (ICP-OES) results of Bi elements in the electrolyte during 3 h electrolysis (unit: ppm) at 1.47 V vs. RHE, Related to Figure 5 and the discussion in main text about the leakage of Bi species

Numbers marked in red indicate unreliable values due to low signal/noise ratio. Bi (306.771) signal shows the best results.

Sample	Bi (190.171)	Bi (222.821)	Bi (223.061)	Bi (306.771)
Blank	0	0	0	0
0 h	Uncal	-0.006656u	0.005886	0.024099
1 h	Uncal	-0.001017u	0.004854	0.028355
2 h	Uncal	0.014216	0.005206u	0.016136
3 h	Uncal	0.013577	0.031695	0.035585

Table S2. Multiple Reaction Monitoring (MRM) parameters for each analyte, Related to Figure 5

	Q1 Mass (Da)	Q3 Mass (Da)	DP (Volts)	EP (Volts)	CE (Volts)	CXP (Volts)
Glyceric acid	105.00	74.900	−60.000	−11.000	−15.800	−11.000
	105.00	56.900	−60.000	−11.000	−19.000	−9.000
Erythronic acid	135.000	117.000	−34.000	−11.000	−13.7000	−11.000
	135.000	75.000	−34.000	−11.000	−17.000	−11.000
Arabinonic acid	165.000	129.000	−50.000	−11.000	−15.3000	−8.000
	165.000	75.000	−50.000	−11.000	−20.000	−13.00
Glucose	179.000	59.000	−50.000	−10.000	−30.000	−30.000
	179.000	88.900	−50.000	−10.000	−15.000	−11.000
Gluconic acid	195.000	129.00	−92.000	−10.000	−18.8000	−11.000
	195.000	75.000	−92.000	−10.000	−25.000	−8.300

Table S3. Catalytic performance comparison of recently developed electrocatalysts for polyol oxidation, Related to Figure 5 and the evaluation of catalytic performance in main text

Catalyst	Polyol	pH	C-C bond breaking	Main products	Ref.
Cu	D-glucose (C6)	13	Yes (0.84 V vs. RHE)	Glucaric acid (C6) Gluconic acid (C6) Formic acid (C1)	(Moggia et al., 2019)
Pt	D-glucose (C6)	13	Yes (0.70 V vs. RHE)	Glucaric acid (C6) Gluconic acid (C6) Formic acid (C1)	(Moggia et al., 2019)
Au	D-glucose (C6)	13	Yes (0.55 V vs. RHE)	Gluconic acid (C6) Formic acid (C1)	(Neha et al., 2021)
Pd3Au7/C	D-glucose (C6)	13	No (voltage of 0.4 V)	Gluconate (C6)	(Rafaïdeen et al., 2019)
PdNi/C	Gluconic acid (C6)	>13	Yes (−0.15 V vs. Hg/HgO)	Hydroxypyruvate (C3) Tartronate (C3) Lactate (C3) Formate (C1) ...	(Martin-Yerga et al., 2021)
Pt9Bi1/C	D-glucose (C6)	13	No (<0.60 V vs. RHE)	Gluconate (C6)	(Neha et al., 2021)
Bi	D-glucose (C6)	13	Yes (1.47 V vs. RHE)	Gluconic acid (C6) Arabinonic acid (C5) Erythronic acid (C4) Glyceric acid (C3)	This work

Transparent Methods

Materials

$Bi(NO_3)_3 \cdot 5H_2O$ ($\geq$ 98.0 %), HNO_3 (60 % aqueous solution), D-(+)-glucose ($\geq$ 99.5 %), D-arabinonic acid sodium salt ($\geq$ 98.0 %), D-erythronic acid potassium salt ($\geq$ 97.0 %), D-glyceric acid sodium salt ($\geq$ 95.0 %), D-gluconic acid solution (49-53 wt.% in H_2O), and KOH ($\geq$ 99.95 %) are purchased from Sigma–Aldrich and used as received. All aqueous solution was prepared using double-deionized water (DI water, R > 18.2 MΩ cm^{-1}) produced by MilliQ Water System (Millipore, USA). Bismuth metal crystal (purity $\geq$ 99.999 %) was provided by American Elements (USA).

Electrochemical deposition of Bi PCs

The Bi PCs-coated glassy carbon electrode (Bi PCs-GCE) was prepared by the overpotential deposition method in Bi^{3+} containing solution (10 mM $Bi(NO_3)_3$ + 0.1 M HNO_3). The GCE was polished firstly with Al_2O_3 (D = 50 nm, CHI) powder for 5 mins to achieve a perfectly smooth surface. The electrochemical deposition was performed using a three-electrode single-compartment configuration with a graphite rod (Union Carbide, <1 ppm impurities) as the counter electrode and saturated calomel electrode (SCE) as the reference electrode. The applied potential of the chronoamperometry was fixed at 0.25 V (*vs*. RHE) for 1000 s. Within 5 mins, a grey coating layer was formed on the GCE surface. The prepared Bi PCs-GCE was washed with DI water four times and used directly for further electrochemical tests.

Laser ablation for Bi NPs production

The Nd:YAG Q-switched pulsed laser (wavelength = 1064 nm, Nimma-600 Laser system) came from Beamtech Optronics Co. Ltd. (China) with an energy output of 650 mJ and energy instability (RMS) $\leq$1 %. Filled with isopropyl alcohol (IPA), the distance between the bulk bismuth target and the liquid surface was fixed at 5 cm, and the beam diameter was *ca*. 0.8 cm. Before the laser ablation, the IPA was purged with Ar for 10 mins to remove dissolved oxygen. During the whole process, the chamber was continuously filled with Ar to avoid potential fire hazards.

Electrochemical characterization

All electrochemical tests were performed with a three-electrode configuration in 0.1 M KOH electrolyte. A graphite rod was used as the counter electrode and a Hg/HgO (1.0 M KOH) as the reference electrode. The cyclic voltammetry (CV) and electrochemical impedance spectroscopy (EIS) experiments were carried out on a PARSTAT MC (PMC 1000/DC, Princeton Applied Research, AMETEK, Inc.) potentiostat. The amperometry and Fourier transformed alternating current voltammetry (FTACV) tests were performed on a CHI760E electrochemical workstation (CH Instruments, Inc.).

For CV measurements, the applied potential started from the open circuit potential (OCP), followed by cathodic polarization to the lowest end of the potential window first and anodic polarization to the highest end.

EIS study was conducted from 1 MHz to 10 mHz with an amplitude of 5 mV at OCP. The potential *vs.* Hg/HgO (1.0 M KOH) reference electrode was converted to the potential *vs.* the reversible hydrogen electrode (RHE) using E (*vs.* RHE) = E (*vs.* Hg/HgO (1.0 M KOH)) + 0.8663 V.

For FTACV, the frequency was 9 Hz, the amplitude was 80 mV, and the data point per Sine was 128. Before the anodic/cathodic scan, the working electrode was held at the initial potential (the lowest potential for the anodic scan; the highest potential for the cathodic scan) for 30 s to ensure the total reduction/oxidation before anodic/cathodic scans.

The long-term electrolysis was performed in a two-compartment electrochemical cell with a counter electrode (graphite rod) separated from the working electrode. The applied potential was 0.60 V (*vs.* Hg/HgO (1.0 M KOH), or 1.47 V *vs.* RHE), and the total electrolysis time was 3 h.

Material characterization

X-ray powder diffraction (XRD) patterns were collected on a SmartLab X-ray diffractometer by Rigaku (voltage 45 kV, current 200 mA). The Bi PCs-coated GCE was used directly for the XRD characterization. The Bi NPs was mixed with AC first, and dried as powder at room temperature for XRD test. Transmission electron microscopic (TEM) images were obtained from a JEOL instrument (Model JEM-2100F, 200 kV). The Bi NPs were used directly for TEM testing without AC addition. Atomic force microscopic (AFM) photos were taken on a Bruker Multimode 8 HR system using the PeakForce Tapping mode with SNL-10 cantilever (silicon tip on nitride lever, k = 0.12 N m^{-1}) and C-AFM was performed using the conducting mode with SCM-PIT-V2 cantilever. The Bi PCs-coated GCE was imaged directly with the GCE substrate, and the Bi NPs (no AC) were drop-cast onto a highly ordered pyrolytic graphite (HOPG) substrate and dried within an N_2-filled enclosure to avoid oxidation. The optical image of the Bi PCs was acquired from the AFM system (the optical microscopy). Inductive coupled plasma optical emission spectrometer (ICP-OES) was conducted on an Agilent 710 series, and the results are shown in **Table S1**. Raman spectra were collected from a Witec confocal Raman system (alpha300 R). The excitation laser (λ = 532 nm) energy was 5 mW for all tests to avoid potential heat damage of samples.

Instrumentation and UPLC–MS/MS conditions

The UPLC–MS/MS analyses were conducted on a Sciex 6500+ Liquid Chromatography/Electrospray Ionization-QTrap Mass Spectrometer. For carboxylic acids analysis, the chromatographic separation was carried out on Waters Acquity UPLC BEH Amide (2.1 mm i.d. × 75 mm, 1.7 μm) column at 60 °C. The mobile phase was 1.5 % formic acid (FA) with 5 mM ammonium formate in H_2O (solvent A), and 1.5 % FA with 5 mM ammonium formate in MeCN/H_2O (v/v = 9:1) (solvent B). The flow rate was set at 0.4 mL min^{-1}. An elution gradient was used as follows: initial elution with 98 % solvent B, followed by a linear gradient to 50 % solvent B from 2.0 to 10.0 min, held at 50 % solvent B from 10.0 to 15.0 min, to 70 % solvent B from 15.0 to 18.0 min, and finally to 98 % solvent B at 20.0 min. For the analysis of glucose, the chromatographic separation was carried on Waters Acquity UPLC BEH HILIC (2.1 mm i.d. × 75 mm, 1.7 μm) column at 60 °C. The mobile phase was 0.05 % NH_4OH with 60 mM ammonium acetate in H_2O (solvent A), and 20 mM ammonium acetate in MeCN/H_2O (v/v = 80:20) (solvent B). The flow rate was set at 0.3 mL min^{-1}. The elution gradient was used as follows: initial elution with 98 % solvent B,

followed by a linear gradient to 50 % solvent B from 2.0 to 10.0 min, held at 50 % solvent from 10.0 to 12.0 min, and, thereafter, to 98 % solvent B at 12.01 min, held at 98% solvent B at 16.0 min. The mass spectrometer was equipped with an electrospray ionization (ESI) source. ESI was performed in negative ion modes. The optimum conditions for the analysis were used as follows: curtain gas pressure 25 psi; vaporizer temperature 550 °C; ion spray voltage −4000 eV; sheath gas pressure 60 psi; auxiliary gas pressure 60 psi. The Multiple Reaction Monitoring (MRM) parameters for each analyte are shown in **Table S2.**

Supplemental references

Martin-Yerga, D., White, J., Henriksson, G., and Cornell, A. (2021). Structure-reactivity effects of biomass-based hydroxyacids for sustainable electrochemical hydrogen production. ChemSusChem. 10.1002/cssc.202100073

Moggia, G., Kenis, T., Daems, N., and Breugelmans, T. (2019). Electrochemical oxidation of d‑glucose in alkaline medium: Impact of oxidation potential and chemical side reactions on the selectivity to d‑gluconic and d‑glucaric acid. ChemElectroChem *7*, 86-95.

Neha, N., Kouamé, B.S.R., Rafaïdeen, T., Baranton, S., and Coutanceau, C. (2021). Remarkably efficient carbon-supported nanostructured platinum-bismuth catalysts for the selective electrooxidation of glucose and methyl-glucoside. Electrocatalysis *12*, 1-14.

Rafaïdeen, T., Baranton, S., and Coutanceau, C. (2019). Highly efficient and selective electrooxidation of glucose and xylose in alkaline medium at carbon supported alloyed PdAu nanocatalysts. Appl. Catal., B *243*, 641-656.